

*Annual Review of Astronomy and Astrophysics*  
**Galaxy Formation and  
Reionization: Key Unknowns  
and Expected Breakthroughs by  
the *James Webb Space Telescope***

Brant E. Robertson

Department of Astronomy and Astrophysics, University of California, Santa Cruz, California,  
USA; email: brant@ucsc.edu

Annu. Rev. Astron. Astrophys. 2022. 60:121–58

First published as a Review in Advance on  
April 8, 2022

The *Annual Review of Astronomy and Astrophysics* is  
online at [astro.annualreviews.org](http://astro.annualreviews.org)

<https://doi.org/10.1146/annurev-astro-120221-044656>

Copyright © 2022 by Annual Reviews.  
All rights reserved

ANNUAL REVIEWS CONNECT

[www.annualreviews.org](http://www.annualreviews.org)

- Download figures
- Navigate cited references
- Keyword search
- Explore related articles
- Share via email or social media

### Keywords

structure formation

### Abstract

The launch of the *James Webb Space Telescope* (JWST) in late 2021 marks a new start for studies of galaxy formation at high redshift ( $z \gtrsim 6$ ) during the era of cosmic reionization. JWST can capture sensitive, high-resolution images and multiobject spectroscopy in the IR that will transform our view of galaxy formation during the first billion years of cosmic history. This review summarizes our current knowledge of the role of galaxies in reionizing intergalactic hydrogen ahead of JWST, achieved through observations with the *Hubble Space Telescope* and ground-based facilities including Keck, the Very Large Telescope, Subaru, and the Atacama Large Millimeter/Submillimeter Array. We identify outstanding questions in the field that JWST can address during its mission lifetime, including with the planned JWST Cycle 1 programs. These findings include the following:

- Surveys with JWST have sufficient sensitivity and area to complete the census of galaxy formation at the current redshift frontier ( $z \sim 8$ –10).
- Rest-frame optical spectroscopy with JWST of galaxies will newly enable measures of star-formation rate, metallicity, and ionization at  $z \sim 8$ –9, allowing for the astrophysics of early galaxies to be constrained.
- The presence of evolved stellar populations at  $z \sim 8$ –10 can be definitively tested by JWST, which would provide evidence of star formation out to  $z \sim 15$ .

## Contents

1. INTRODUCTION .....	122
2. PHYSICAL COMPONENTS OF COSMIC REIONIZATION .....	124
2.1. Constraining the Reionization Process .....	124
2.2. Lyman Continuum Escape Fraction .....	125
2.3. Physics of Lyman Continuum Escape .....	127
2.4. Indirect Measures of Lyman Continuum Escape .....	127
2.5. Ionizing Photon Production Efficiency .....	128
2.6. Luminosity Density .....	130
2.7. Evolution of the Ionized Fraction .....	134
3. MODELS OF HIGH-REDSHIFT GALAXY FORMATION AND REIONIZATION .....	137
4. ROLE OF ACTIVE GALACTIC NUCLEI AND QUASARS .....	138
5. INNOVATIONS IN HIGH-REDSHIFT GALAXY OBSERVATIONS .....	139
5.1. Gravitationally Lensed Observations .....	140
5.2. Pure-Parallel Surveys .....	140
5.3. ALMA Observations of High-Redshift Galaxies .....	141
6. HIGH-REDSHIFT GALAXY STELLAR MASS CONSTRAINTS .....	141
7. SPECTROSCOPY OF THE HIGHEST-REDSHIFT GALAXIES .....	142
7.1. Spectroscopic Confirmation of Distant Galaxy Redshifts .....	142
7.2. Spectroscopic Probes of Reionization-Era Galaxy Astrophysics .....	144
8. FUTURE PROGRESS WITH JWST .....	144
8.1. Overview of JWST Instrumentation .....	144
8.2. JWST Programs .....	146
9. SUMMARY .....	150

## 1. INTRODUCTION

Ever deeper observations continue to reveal the earliest epochs of galaxy formation. Searches for distant galaxies now probe the era of cosmic reionization, when hydrogen in the intergalactic medium (IGM) transitioned from neutral to ionized, and reach well past its conclusion at redshift  $z \sim 6$  about 1 billion years after the Big Bang. By discovering galaxies in the first few hundred million years of cosmic time and measuring their properties, we can study the connection between galaxy formation and cosmic reionization. With the launch of the *James Webb Space Telescope* (JWST) in late 2021, observations of galaxies during cosmic reionization will advance dramatically. This review surveys present progress in relating galaxies with cosmic reionization and previews discoveries with JWST that will transform our understanding of how early galaxies form and affect intergalactic hydrogen.

To date, sensitive observations with the *Hubble Space Telescope* (HST) have detected candidate galaxies photometrically with plausible redshifts as high as  $z \sim 11$ . The most distant galaxies with spectroscopically confirmed redshifts lie at redshifts  $z \sim 9\text{--}10$ , with spectra taken by the Keck Telescope, the Very Large Telescope (VLT), and the Atacama Large Millimeter/submillimeter Array (ALMA). At slightly lower redshifts  $z \sim 7\text{--}9$ , photometric surveys have provided  $\sim 1,000$  galaxy candidates to date. Of these, direct spectroscopic confirmation exists for  $\sim 100$  at  $z \sim 7$  and a handful at  $z > 8$ . The majority of these photometric and spectroscopic discoveries occurred over the past decade since the installation of the HST Wide Field Camera 3 (WFC3) in May 2009, as

the new sensitivity, field of view, filter array, and resolution of WFC3 relative to its Near Infrared Camera and Multi-Object Spectrometer predecessor improved the capabilities of HST to detect and select high-redshift galaxies. The combination of HST and the *Spitzer Space Telescope* enabled the first simultaneous measurements of the rest-frame ultraviolet (UV) and optical spectral energy distributions of distant galaxies, allowing for joint inferences of the star-formation rates (SFRs) and stellar masses of early-forming systems. Using the arsenal of observational facilities available to date, we have inferred the SFR, stellar mass, gas content, metallicity, and dust content in collections of galaxies at redshifts  $z > 6$ . With the new capabilities afforded by JWST, the search for the most distant galaxies will again be reinvigorated. Relative to HST or *Spitzer*, JWST features a much larger collecting area, instruments sensitive to wavelengths  $\lambda \sim 1\text{--}28 \mu\text{m}$ , and multiplexed spectroscopic capabilities. JWST will provide a completely new view on cosmic reionization.

The study of high-redshift galaxies often connects with the novelty of finding the most distant or earliest-forming systems. Such discoveries provide mileposts in our exploration of the nascent Universe, where observationally we have established the presence of virialized structures that managed to host star formation. Given the technical challenge of detecting faint distant objects, measuring their fluxes photometrically, and using spectroscopy to constrain the finer details of their emission, the process of discovering the earliest galaxies requires a substantial scientific endeavor with its own value. Beyond their discovery, the characteristics of individual objects provide a wealth of information about the physics of galaxy evolution in the context of cosmological structure formation. **Figure 1** provides an illustrative diagram of the history of galaxy evolution, highlighting the epoch of cosmic reionization at redshifts  $z \sim 6\text{--}12$ . In addition

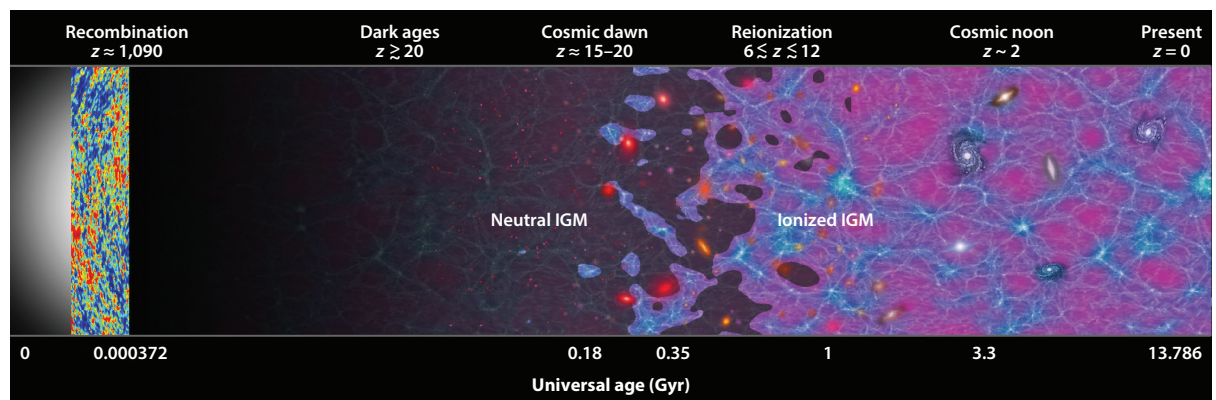


**Figure 1**

Overview of universal history highlighting the epoch of reionization. After the Big Bang ( $t = 0$ ), the Universe expanded and cooled until electrons could recombine with protons to form neutral hydrogen ( $z \approx 1,090$  at  $t \approx 372,000$  years). During the subsequent Dark Ages, the Universe remained dim and neutral until the first stars formed at Cosmic Dawn, with substantial galaxies forming likely after  $z \sim 20$  ( $t \approx 180$  Myr) and perhaps as late as  $z \sim 15$ . Once galaxies grew in abundance and luminosity, such that their escaping Lyman continuum radiation could begin to ionize the surrounding IGM, the process of cosmic reionization commenced. Over the period of redshifts  $12 \lesssim z \lesssim 6$ , corresponding to times  $0.35 \lesssim t \lesssim 1$  Gyr, hydrogen in the bulk IGM transitioned from a nearly completely neutral to a nearly completely ionized state. The figure illustrates the changing ionization state of the IGM as a patchy transition between shaded and unshaded regions, with the corresponding evolution of the galaxy populations represented with simple model images. After cosmic reionization, star light and radiation from active galactic nuclei (AGNs) maintained the ionization of the IGM through the peak of cosmic star formation at Cosmic Noon ( $z \sim 2$  and  $t \approx 3.3$  Gyr) to the present ( $z = 0$  at  $t = 13.786$  Gyr). This correspondence between redshift and time assumes the Planck Collab. et al. (2020) best-fit cosmology. Figure adapted from Robertson et al. (2010). Abbreviation: IGM, intergalactic medium.

to the many discoveries JWST will provide for galaxies during the last 13 billion years of cosmic time, JWST can push our knowledge back beyond the height of cosmic reionization to the eras when the very earliest galaxy forms. Given this context for discoveries, the launch of JWST prompts several questions. What are the critical properties of the high-redshift galaxy population that can be measured with JWST, and why are they interesting? How well have prior facilities constrained the abundance and properties of high-redshift galaxies? What do we know about the impact of galaxy formation on the cosmic reionization process that transitioned the neutral IGM to an ionized state by  $z \sim 6$ ? Importantly, how can JWST improve our knowledge, and what new questions can observations with JWST resolve that have been previously unanswerable to date?

We provide the physical motivations for the study of high-redshift galaxy populations and outline what measurements provide critical insight. We summarize the progress achieved in understanding high-redshift galaxies with HST and contemporary observations. We review the capabilities and instrumentation that will allow JWST to make further discoveries, connecting the capabilities of the instrument to scientific questions they can optimally address. We conclude by reviewing the observing programs to be conducted during JWST Cycle 1 that will contribute to answering the outstanding scientific questions our present facilities have not yet solved. For a detailed summary of the discoveries of HST and *Spitzer* for early galaxies, we point the reader to Stark (2016). For a review of the evolving properties of the IGM, see McQuinn (2016). A recent relevant overview of Ly $\alpha$ -emitting galaxies has been produced by Ouchi et al. (2020).

## 2. PHYSICAL COMPONENTS OF COSMIC REIONIZATION

JWST can pursue several important goals in characterizing the contribution of galaxies to cosmic reionization. These efforts include taking a census of the UV radiation supplied by early star-forming galaxies, providing indirect constraints on the Lyman continuum (LyC) photon production rate of distant galaxies, contributing to any possible lever on the LyC escape fraction, and detecting the possible presence of evolved stellar populations indicating prior star formation to very high redshifts. Below, we discuss how cosmic reionization may be constrained and review the current empirical evidence from HST and other facilities for the contribution of star-forming galaxies.

### 2.1. Constraining the Reionization Process

The term reionization encapsulates the complex process of transitioning intergalactic hydrogen gas from a mostly neutral to a nearly fully ionized state. Classically, this process has been represented by the average volume-filling fraction of ionized gas  $Q_{\text{HII}}(z)$  (e.g., Madau et al. 1999). Connecting the ionized fraction  $Q_{\text{HII}}$  with the properties of the earlier galaxy population amounts to tracking the balance of ionizations and recombinations in the IGM where star-forming galaxies and active galactic nuclei (AGNs) drive the ionization by supplying LyC photons. The process of cosmic reionization involves a complex interplay among the star formation in galaxies, the character of stellar populations that form, the interior structure of interstellar gas in galaxies, the ionization fraction of the circumgalactic medium around galaxies, the evolving mean free path of ionizing radiation in the IGM and both the current strength and history of background radiation from distant sources. For the purposes of connecting reionization to the galaxy population, and using that connection as motivation in part to explore the status of current high-redshift observations and future promise of JWST observations, the hydrogen ionization fraction  $Q_{\text{HII}}$  will be treated as a global quantity averaged over large scales. The ionization fraction  $Q_{\text{HII}}$  is primarily influenced by a competition between the production rate of ionizing photons and hydrogen recombinations.

Crudely, for star-forming galaxies this production of ionizing photons can be captured by the relation,

$$\dot{n}_{\text{ion}} = f_{\text{esc}} \xi_{\text{ion}} \rho_{\text{UV}}, \quad 1.$$

where  $\rho_{\text{UV}}$  is the comoving total UV luminosity density ( $\text{erg s}^{-1} \text{Hz}^{-1} \text{Mpc}^{-3}$ ),  $f_{\text{esc}}$  is the fraction of LyC photons that escape galaxies to ionize intergalactic hydrogen, and  $\xi_{\text{ion}}$  is the ionizing photon production efficiency ( $\text{Hz erg}^{-1}$ ) that indicates the number of LyC photons per unit UV luminosity density the stellar populations in galaxies generate. The quantity  $\dot{n}_{\text{ion}}$  represents the comoving density of LyC photons produced per unit time available for ionizing hydrogen in the IGM.

## 2.2. Lyman Continuum Escape Fraction

Constraints on the LyC escape fraction during the reionization era are indirect. The opacity of the IGM to ionizing radiation increases dramatically with redshift (Madau 1995, Inoue et al. 2014), effectively preventing the direct detection of LyC photons for galaxies above  $z \sim 4.5$  and making observations at  $z \sim 2-4$  difficult. Nonetheless, substantial effort has been invested in performing direct observations of the LyC spectroscopically and photometrically, both in detecting individual sources and by stacking multiple nondetections. The vital inferences about LyC escape at  $z \sim 2-4$  enabled by these efforts can then be applied, with caution, to analogous galaxies present at  $z \gtrsim 6$  with the hope of at least motivating assumptions on  $f_{\text{esc}}$  during reionization.

The reliable detection of rest-frame LyC in distant galaxies proves challenging owing to the possible foreground contamination by objects at lower redshifts. The LyC flux of an object can be measured via photometry or spectroscopy blueward of  $\lambda = 912 \text{ \AA}$ . The potential of interlopers means that high-resolution imagery, such as that provided by HST, is a key component of LyC direct detection campaigns. HST provides the ability to resolve nearly coincident interlopers using nonionizing flux (Mostardi et al. 2015, Shapley et al. 2016, Pahl et al. 2021) and to assess directly the LyC with reduced fear of contamination (Siana et al. 2015, Vasei et al. 2016, Rutkowski et al. 2017, Fletcher et al. 2019). Ground-based imaging in  $U$ -band or similar filters remains an attractive approach for constraining LyC at high-redshift, given their acceptable efficiency and availability on large telescopes (Guaita et al. 2016, Naidu et al. 2018, Meštrić et al. 2020). Imaging redshifted LyC also benefits from spectroscopic redshifts by preventing nonionizing photons from a source at an uncertain distance from contaminating the inference of escaping ionizing flux or at least quantifying the degree of contamination. Given the large intrinsic ratio of nonionizing to ionizing flux in the rest-frame UV spectra of these galaxies, and the small expected escape fractions, even a small amount of nonionizing flux mistaken as LyC can render conclusions about  $f_{\text{esc}}$  unreliable. Spectroscopic determinations do not suffer from this uncertainty, but LyC campaigns with ground-based slit spectrographs are in principle not immune to foreground contamination. Perhaps a bigger practical challenge is conducting large campaigns with blue-sensitive spectrographs, which involves either the HST Cosmic Origins Spectrograph (COS) at low redshift (Izotov et al. 2016a,b, 2018) or significant investment with instruments like VLT/VIMOS (VIable Multi-Object Spectrograph) (de Barros et al. 2016; Marchi et al. 2017, 2018) or Keck/LRIS (Low Resolution Imaging Spectrometer) (Shapley et al. 2016, Steidel et al. 2018). For all high-redshift observations, careful consideration of the effects of absorption by the intervening IGM is required, including potential variations in the transmission along different lines of sight (e.g., Shapley et al. 2016, Bassett et al. 2021).

Constraints on the escape fraction of LyC photons have varied widely with redshift. (We discuss “absolute” escape fractions unless otherwise noted.) Through HST images of resolved stars in the  $z \sim 0$  galaxy NGC 4214, Choi et al. (2020) determine an escape fraction of

$f_{\text{esc}} \approx 0.25$ , noting that differences with previous measurements finding  $f_{\text{esc}} \sim 0$  could be accounted for by viewing angle and geometrical effects. Using HST/COS observations of relatively nearby ( $z \lesssim 0.3$ ) galaxies, the LyC escape fractions measured are reported in the range of  $f_{\text{esc}} \sim 0.06$ – $0.35$  (Izotov et al. 2016a,b, 2018, 2021). *Galaxy Evolution Explorer* (GALEX)-based LyC constraints provide  $f_{\text{esc}} \lesssim 0.021$ – $0.095$  at  $z \sim 1$  (Rutkowski et al. 2016). Observations with the HST Solar Blind Channel provide limits of  $f_{\text{esc}} \lesssim 0.04$ – $0.13$  for individual objects at  $z \sim 1.3$  (Alavi et al. 2020). Stacks of GALEX nondetections provide limits of  $f_{\text{esc}} \lesssim 0.028$  at  $z \sim 2.2$  (Matthee et al. 2017), whereas nondetections in HST F275W imaging provide  $f_{\text{esc}} \lesssim 0.056$  at  $z \sim 2.5$  (Rutkowski et al. 2017). Using the Hubble Deep UV Legacy Survey, Jones et al. (2021) detect LyC from five F275W sources at  $2.35 < z < 3.05$  and conclude galaxies in this redshift range could maintain the IGM ionization state. Smith et al. (2020) use UV HST imaging in Great Observatories Origins Deep Survey (GOODS) to measure  $f_{\text{esc}} \simeq 0.28^{+0.20}_{-0.04}$  for AGNs at  $z \sim 2.3$ – $4.3$ . Through searches of HST UV images of the Ultra Deep Field, Japelj et al. (2017) place relative escape fraction limits of  $f_{\text{esc, rel}} < 0.07$  for faint galaxies at  $z \sim 3$ – $4$ . At higher redshift  $z \sim 3$ , more individual detections have been possible (e.g., Mostardi et al. 2015, Vanzella et al. 2016). The sample-averaged escape fraction from a dozen individual detections at  $z \sim 3$  has been reported as  $f_{\text{esc}} = 0.06 \pm 0.01$  from the Keck Lyman Continuum Spectroscopic Survey augmented with HST imaging (Pahl et al. 2021; updating from  $f_{\text{esc}} = 0.09 \pm 0.01$  measured by Steidel et al. 2018). At  $z \sim 3.1$ , the LymAn Continuum Escape Survey (LACES) measured HST F336W photometry for 61 strong line-emitting sources, finding an average escape fraction of  $f_{\text{esc}} \sim 0.2$  for detected sources and limits in nondetected sources of  $f_{\text{esc}} \lesssim 0.005$  (Fletcher et al. 2019). LyC detection from long-duration gamma-ray burst host galaxies at  $z \sim 3$ – $3.5$  implies escape fractions of  $f_{\text{esc}} \approx 0.08$ – $0.35$  (Vielfaure et al. 2020). A remarkable individual LyC detection at  $z = 4$  with VLT/FORS (FOcal Reducer/low dispersion Spectrograph) suggests a relative escape fraction of  $f_{\text{esc, rel}} = 0.5$ – $1.0$  (Vanzella et al. 2018).

Given the range of measurements for  $f_{\text{esc}}$  over a wide range of redshifts  $z \lesssim 4$ , definitive conclusions about LyC escape during cosmic reionization at  $z \gtrsim 6$  are difficult to draw. The direct measurement of LyC is critical in establishing the reality of ionizing flux escaping from galaxies, but the process of LyC and its connection to other observables needs to be understood to extrapolate measurements at  $z \lesssim 4$  to the era of cosmic reionization. Other methods for estimating  $f_{\text{esc}}$  for more distant objects are needed. Cross-correlations between galaxies and IGM transmissivity in sightlines to distant quasars have enabled the inference of an escape fraction of  $f_{\text{esc}} = 0.23^{+0.46}_{-0.12}$  for star-forming galaxies at  $z \sim 5.5$ – $6.4$  (Kakiichi et al. 2018, Meyer et al. 2020). Experiments measuring redshifted 21-cm signals will provide an indirect handle on  $f_{\text{esc}}$  via constraining the impact of galaxies on the evolving properties of the IGM (e.g., The HERA Collab. et al. 2022a,b). Consistency checks between the strength of observed nebular emission from high-redshift galaxies, which is powered by the ionization of the interstellar medium (ISM) by LyC emission internal to galaxies, the escape fraction, and the character of the stellar population expressed by  $\xi_{\text{ion}}$ , can be performed. However, without direct LyC detections the model-independent inference of  $f_{\text{esc}}$  will likely remain elusive for high-redshift galaxies.

The predicted extreme absorption by the IGM suggests a high improbability of reliable direct detections of LyC emission during cosmic reionization. To connect direct LyC observations at lower redshifts with the reionization process, the physics of LyC production and escape need to be understood. As the physical process of LyC escape becomes clearer, observed correlations among the inaccessible  $f_{\text{esc}}$ , the production efficiency of ionizing photons  $\xi_{\text{ion}}$ , and observationally accessible signatures can be used to interpret more confidently how leaking LyC from high-redshift galaxies reionizes intergalactic hydrogen.

### 2.3. Physics of Lyman Continuum Escape

For understanding the physics of LyC escape, astrophysical simulations play a critical role. Large-scale simulations that predict how the properties of the galaxy population evolve during cosmic reionization are presented in Section 3. Here, we highlight a few detailed simulations of LyC escape in galaxies directly relevant for understanding how  $f_{\text{esc}}$  is determined rather than studying its implications. Using radiative transfer applied to zoom-in simulations of galaxy formation coupled with synthesis models for predicting the emission from stellar populations, Ma et al. (2016, 2020) found that feedback from star formation supports an escape fraction of  $f_{\text{esc}} \approx 0.2$ . In high-mass galaxies, dust reduces  $f_{\text{esc}}$ , whereas at the extreme low-mass end  $f_{\text{esc}}$  again decreases owing to the inefficiency of feedback in creating escape paths for ionizing radiation. Using radiative transfer postprocessing of zoom-in cosmological simulations including a detailed model for feedback, Barrow et al. (2020) found that when LyC escapes from star-forming galaxies it does so through low column sightlines affected by prior feedback from star formation. Computing possible observable signatures associated with high  $f_{\text{esc}}$ , they found that while high  $f_{\text{esc}}$  occurs during periods of strong  $[\text{OIII}]/[\text{OII}]$  line ratios associated with ionizing input from massive stars, the converse was not necessarily true and that no direct causal connection existed between strong  $[\text{OIII}]/[\text{OII}]$  and  $f_{\text{esc}}$  (see also Izotov et al. 2017 for a similar observational inference). In radiation hydrodynamical simulations with  $<5$ -pc resolution, Secunda et al. (2020) found that because periods of high  $f_{\text{esc}}$  follow vigorous star-formation episodes by  $\sim 100$  Myr, the delayed increase in ionizing photons associated with binary evolution after the initial stellar formation leads to an increased photon-weighted mean escape fraction of  $f_{\text{esc}} \approx 0.17$ . Zoom-in cosmological simulations including radiative hydrodynamics can be used to predict the connection between  $f_{\text{esc}}$  and near-UV lines, and CII 1334 Å flux correlates well with  $f_{\text{esc}}$  after correcting for dust attenuation (Mauerhofer et al. 2021). Using semianalytical models, Seiler et al. (2018) found enhanced  $f_{\text{esc}}$  for intermediate-mass galaxies in which phases of AGN feedback could affect the subsequent ability of ionizing photons to escape. On much smaller scales, using radiation hydrodynamical simulations of LyC escape from HII regions, Kakiichi & Gronke (2021) found that LyC photons leak through low column density regions in the turbulent ISM. Supersonic turbulence in the ISM associated with star-forming clouds leads to a wide density and surface density distribution, providing low column pathways for ionizing photons to escape even before supernovae feedback.

### 2.4. Indirect Measures of Lyman Continuum Escape

Constructing observational measures of LyC escape that do not rely on direct detection of LyC emission are essential for understanding the reionization era. These techniques will prove increasingly important during JWST operations, as rest-frame optical spectra will become a standard tool during the study of galaxies during cosmic reionization. Related indirect measures of the ionizing photon efficiency  $\xi_{\text{ion}}$  are discussed in Sections 2.5 and 7.2. Here, we review studies of indirect measures of  $f_{\text{esc}}$  in galaxies.

Local observations have provided interesting test beds for studying the connection between  $f_{\text{esc}}$  and other galaxy properties. Alexandroff et al. (2015) found that for a sample of far-UV COS-observed galaxies, LyC leakiness most strongly correlated with Ly $\alpha$  equivalent width. Local galaxy observations with COS suggest that LyC  $f_{\text{esc}}$ , the escape of Ly $\alpha$ , and the Ly $\alpha$  equivalent width are connected (Izotov et al. 2018, 2020), but no clear connection between high  $[\text{OIII}]/[\text{OII}]$  and high  $f_{\text{esc}}$  has been found. Escape fractions in these objects decrease with increasing velocity separation between the peaks of Ly $\alpha$  emission, and this relationship has been used to estimate an escape fraction of  $f_{\text{esc}} \approx 0.59$  in the lensed  $z = 6.803$  galaxy A370p-z1 (Meyer et al. 2021). Regarding the possible role of outflows in increasing  $f_{\text{esc}}$ , Chisholm et al. (2017) found that LyC leaking galaxies fell on

the low side of the equivalent width distribution of absorption lines tracing outflows, suggesting low metallicities and low H $\text{I}$  column densities. Using UV Lyman series lines and low-ionization metal absorption lines, Chisholm et al. (2018) found that H $\text{I}$  and ISM absorption lines could be used to predict  $f_{\text{esc}}$  in low-redshift LyC leakers. Recently, using a sample of more than a dozen confirmed LyC-emitting, mostly low-redshift galaxies, Gazagnes et al. (2020) determined correlations between low neutral gas covering fraction  $f_{\text{cov}}$ , low Ly $\alpha$  peak velocity separations, and high  $f_{\text{esc}}$ .

At higher redshifts, both optical emission and ISM absorption have been connected to  $f_{\text{esc}}$ . Using almost a thousand  $z \sim 3$  galaxies, Reddy et al. (2016) established an empirical correlation between the reddening  $E(B - V)$  and neutral gas covering fraction  $f_{\text{cov}}$ . If the absolute LyC escape fraction is  $f_{\text{esc}} \approx 1 - f_{\text{cov}}$ , then reddening and  $f_{\text{esc}}$  can be related and estimated in distant galaxy populations. In their spectral analysis at  $z \sim 3$ , Steidel et al. (2018) found a strong correlation between  $f_{\text{esc}}$  and Ly $\alpha$  equivalent width, which induced a residual correlation between  $f_{\text{esc}}$  and UV luminosity. Using rest-frame optical spectra of the  $z \sim 3$  LyC leaking galaxies from LACES, Nakajima et al. (2020) demonstrated an empirical connection between large [OIII/OII] emission line ratios and large  $f_{\text{esc}}$  in their sample. In principle, any of these methods could be honed for applications to high-redshift galaxy populations, especially as multiplexed IR spectroscopy from JWST is a near-term possibility.

## 2.5. Ionizing Photon Production Efficiency

The quantity  $\xi_{\text{ion}}$  provides a translation between the observable rest-frame UV emission from galaxies and the corresponding number of LyC photons their stars produce. If the LyC emission from galaxies was directly observable in the reionization era, the product  $f_{\text{esc}} \xi_{\text{ion}} L$  from a single galaxy could be replaced by the emergent LyC luminosity  $L_{\text{ion}}$  normalized by average photon energy to get the number of LyC photons each galaxy releases. Instead, the proxy  $\xi_{\text{ion}}$  is used to reflect how the observed UV spectrum of the galaxy is expected to extend blueward of  $\lambda = 912 \text{ \AA}$ . The expectations for  $\xi_{\text{ion}}$  are model dependent, as they rely on the initial mass function (IMF) of stars, the galaxy's star-formation history, the evolution of individual stars, stellar metallicity that affects their mass-loss rates and sizes, and potential stellar binary interactions (e.g., Zackrisson et al. 2011, 2013, 2017; Eldridge et al. 2017; Stanway & Eldridge 2018, 2019). In what follows, we use the binary population and spectral synthesis model (hereafter BPASS; Eldridge et al. 2017, v2.2 used throughout) to explicate the connection among metallicity, binarity, and the ionizing photon production efficiency  $\xi_{\text{ion}}$ .

Metallicity influences ionizing photon production efficiency in several ways. The amount of mass loss to stellar winds depends on the stellar metallicity by changing the atmospheric opacity. Stars that lose mass through winds also lose angular momentum, which in turn reduces the replenishment of fuel through rotational mixing. The high-metallicity stars then burn slower at lower temperatures over longer timescales than low-metallicity stars. Metallicity also has a strong effect on the importance of binary interactions. As discussed by Eldridge et al. (2017), binary star interactions lead to substantial mass transfer from the primary to the secondary star. The accretion of mass onto the secondary can lead to an increased rotation rate and, if more than  $\sim 5\%$  of the initial stellar mass is accreted, the rotation will lead to rotational mixing of fuel inside the star and more vigorous burning. The result is a substantial increase in the ionizing photon production rate relative to singleton stars. High-metallicity stars lose more mass to stellar winds, which leads to more compact older stars and less mass transfer in binary interactions. By combining a detailed description of these physics with a model for the fraction of stars that occur in binaries and the distribution of binary orbits, the resulting enhancement to the overall ionizing photon production efficiency of the population owing jointly to metallicity and binary interactions can be computed.

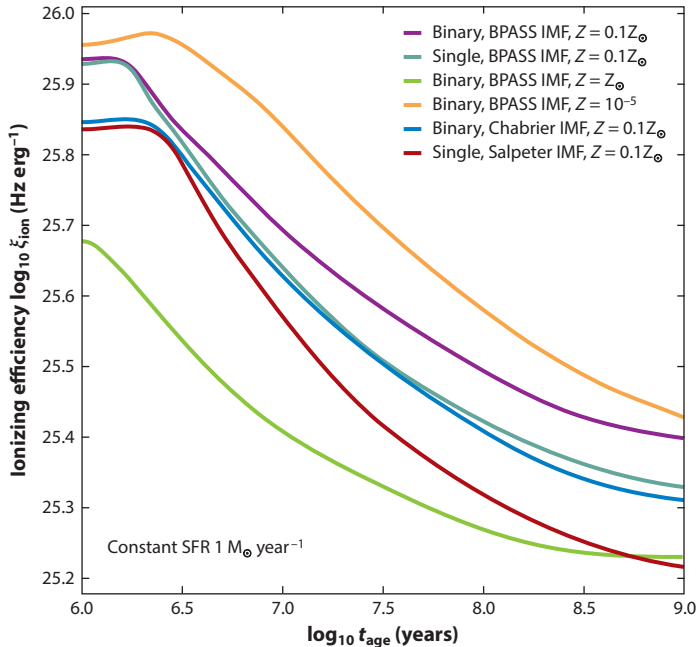


**Figure 2**

Ionizing photon production efficiency  $\xi_{\text{ion}}$  as a function of stellar population age in the BPASS population synthesis models (Eldridge et al. 2017; Stanway & Eldridge 2018, 2019). Shown is the ratio  $\xi_{\text{ion}} \equiv N_{\text{ion}} / L_{1500\text{\AA}}$  with units ( $\text{Hz erg}^{-1}$ ), where  $N_{\text{ion}}$  and  $L_{1500\text{\AA}}$  are, respectively, the number of ionizing photons per second and the specific UV luminosity near 1500 Å produced by a constant star-formation rate population with age  $t_{\text{age}}$ . The model predictions cover both single and binary star evolution that affect the predicted temperature of massive stars, as well as metallicity effects that cause low-metallicity stars to prove more efficient at producing ionizing radiation than higher-metallicity stars. The ionizing photon production is also influenced by the IMFs with the default BPASS Eldridge et al. (2017), Chabrier (2003), and Salpeter (1955) IMF model predictions shown for  $Z = 0.1 Z_{\odot}$  metallicity. Note that these curve labels assume  $Z_{\odot} \equiv 0.02$ . Abbreviations: BPASS, binary population and spectral synthesis model; IMF, initial mass function.

**Figure 2** shows the evolution of  $\xi_{\text{ion}}$  predicted by BPASS for a dust-free galaxy with a constant SFR as a function of stellar population age  $t_{\text{age}}$ . Shown are models with (“Binary”) and without (“Single”) binary interactions, with different metallicities  $Z$  relative to the solar value (assumed here to be  $Z_{\odot} = 0.02$ ). The production of ionizing photons depends on the presence of massive stars and therefore the IMF. In BPASS, the IMF is modeled as a broken power law such that the number of stars with masses less than a maximum mass  $m_{\text{max}}$  is given by

$$N(m < m_{\text{max}}) \propto \int_{0.1}^{m_1} \left( \frac{m}{M_{\odot}} \right)^{\alpha_1} dm + m_1^{\alpha_1} \int_{m_1}^{m_{\text{max}}} \left( \frac{m}{M_{\odot}} \right)^{\alpha_2} dm, \quad 2.$$

where  $m_1$  is the mass where the power law breaks, and  $\alpha_1$  and  $\alpha_2$  are the power-law slopes for low-mass and high-mass stars, respectively. The default BPASS IMF has  $\alpha_1 = -1.3$ ,  $\alpha_2 = -2.35$ ,  $m_1 = 0.5 M_{\odot}$ , and  $m_{\text{max}} = 300 M_{\odot}$ . In this formulation, the Salpeter (1955) IMF is a continuous power law with  $\alpha_1 = \alpha_2 = -2.35$ . The Chabrier (2003) has a modified exponential cut-off at low masses ( $m_1 = 1 M_{\odot}$ ) and a slightly shallower high mass slope ( $\alpha = 2.3$ ). The models in **Figure 2** assume a maximum mass  $m_{\text{max}} = 100 M_{\odot}$  for the Salpeter (1955) and Chabrier (2003) IMF models.

The differences in  $\xi_{\text{ion}}$  with binarity, metallicity, IMF, and population are substantial (Stanway et al. 2016). For binary models, low-metallicity populations produce 2–3× more ionizing photons

per unit UV luminosity than solar metallicity populations. At fixed metallicity, binary interactions increase  $\xi_{\text{ion}}$  by about 25% at  $t_{\text{age}} = 100$  Myr. At fixed metallicity, the default BPASS IMF results in a higher  $\xi_{\text{ion}}$  than Chabrier (2003) also by  $\approx 25\%$ . For reference, a stellar population of age  $t_{\text{age}} \sim 100$  Myr and metallicity of  $Z = 0.1 Z_{\odot}$  will have  $\log_{10}(\xi_{\text{ion}}/\text{Hz erg}^{-1}) \approx 25.46$ . For a metallicity of  $Z = 0.005 Z_{\odot}$ ,  $\log_{10}(\xi_{\text{ion}}/\text{Hz erg}^{-1}) \approx 25.60$ . Direct metallicity constraints from ALMA O<sub>III</sub> 88  $\mu\text{m}$  at  $z > 7$  indicate  $Z \approx 0.2 Z_{\odot}$  (Jones et al. 2020), such that large  $\xi_{\text{ion}}$  should be possible. The  $\xi_{\text{ion}}$  of the entire population will depend on the collection of star-formation histories from individual objects. For instance in the BLUETIDES simulations, Wilkins et al. (2016) found variations in the star-formation histories and metal enrichment in high-redshift galaxies led to  $\log_{10}(\xi_{\text{ion}}/\text{Hz erg}^{-1}) \approx 25.1\text{--}25.5$ .

From the strength of nebular emission powered by reprocessed LyC, observations can provide estimates of  $\xi_{\text{ion}}$ . At  $z \sim 2$ , estimates of  $\xi_{\text{ion}}$  from UV complete samples with H $\alpha$  spectroscopy give  $\log_{10}(\xi_{\text{ion}}/\text{Hz erg}^{-1}) \approx 25.47$  (Emami et al. 2020). The MOSDEF [MOSFIRE (Multi-Object Spectrometer for Infra-Red Exploration) Deep Evolution Field] has constrained ionizing photon production spectroscopically at  $z \sim 2$ , finding a lower limit of  $\log_{10}(\xi_{\text{ion}}/\text{Hz erg}^{-1}) \approx 25.06\text{--}25.34$  depending on the dust model, with elevated  $\xi_{\text{ion}}$  in galaxies with high [O<sub>III</sub>]/H $\beta$  or with UV continuum slopes  $\beta < -2.1$  (Shivaei et al. 2018). Star-forming galaxies at redshifts  $z \sim 2\text{--}3$  often show increased Ly $\alpha$  equivalent widths with increasing [O<sub>III</sub>]/H $\beta$ , indicating a connection between enhanced ionizing photon production efficiency and escape (Tang et al. 2020). At redshift  $z \sim 3.1\text{--}3.7$ , Nakajima et al. (2016) and Onodera et al. (2020) found evidence for ionizing photon production efficiencies as high as  $\log_{10}(\xi_{\text{ion}}/\text{Hz erg}^{-1}) \approx 25.8$  in strong-emission line galaxies. Observational estimates of  $\xi_{\text{ion}}$  at  $z \sim 4\text{--}5$ , where H $\alpha$  nebular emission is still probed by *Spitzer* broadband colors, provide values of  $\log_{10}(\xi_{\text{ion}}/\text{Hz erg}^{-1}) \approx 25.36\text{--}25.8$  (Bouwens et al. 2016, Lam et al. 2019), with strongest  $\xi_{\text{ion}}$  values in objects with blue UV continua ( $\beta < -2.3$ ). The same approach can be applied out to very high redshift using the enhanced *Spitzer* coverage of GOODS from the GREATS (GOODS Re-ionization Era wide-Area Treasury from Spitzer) survey, and De Barros et al. (2019) measured  $\log_{10}(\xi_{\text{ion}}/\text{Hz erg}^{-1}) \approx 25.77$  for early galaxies at  $z \sim 8$ . Possible AGN contributions to these ionizing photon production efficiencies can in principle be determined by measuring rest-UV spectral lines, comparing the collisionally excited metal lines with the He 1640  $\text{\AA}$  recombination line or by using UV Ne line diagnostics (Feltre et al. 2016).

## 2.6. Luminosity Density

The total UV luminosity density  $\rho_{\text{UV}}$  provides an observable handle on the cosmic SFR density  $\dot{\rho}_{\star}$ , as the rest-frame UV emission from a galaxy is connected to the presence of newly formed massive stars (see the review by Madau & Dickinson 2014). The luminosity density  $\rho_{\text{UV}}$  depends on the integral of the luminosity function  $\Phi(L) \equiv dn/dL$  weighted by the UV luminosity  $L$  (a luminosity density in the rest-frame UV, typically taken near  $\lambda = 1500 \text{\AA}$ , with units  $\text{erg s}^{-1} \text{Hz}^{-1}$ ) as

$$\rho_{\text{UV}} = \int_0^{\infty} \Phi(L)L \, dL, \quad 3.$$

where the formal limits  $[0, \infty]$  are effectively truncated at low and high luminosities by the physics of galaxy formation that determine the functional form of  $\Phi(L)$ . Indeed,  $\rho_{\text{UV}}$  is finite, even as the observed shape of  $\Phi$ , typically close to a Schechter (1976) function,

$$\Phi(L) = \phi_{\star} \left( \frac{L}{L_{\star}} \right)^{\alpha} \exp \left( -\frac{L}{L_{\star}} \right) d \left( \frac{L}{L_{\star}} \right), \quad 4.$$

can approach a divergent faint-end slope  $\alpha = -2$  over the range of observed luminosities. In terms of the UV absolute magnitude  $M_{\text{UV}}$ , the Schechter (1976) function can be written as

$$x \equiv 10^{-0.4(M_{\text{UV}} - M^*)}, \quad 5.$$

$$\phi(M_{\text{UV}}) = 0.4 \ln 10 \phi^* x^{(\alpha+1)} \exp(-x), \quad 6.$$

where typically we find the normalization  $\phi^* \lesssim 10^{-3}$  ( $\text{Mpc}^{-3} \text{ mag}^{-1}$ ) and the characteristic magnitude  $M^* \approx -21$  at  $z \gtrsim 6$ . The functional form (Equations 4 and 5) should be considered approximate, as eventually at low enough luminosities the efficiency of galaxy formation should truncate the abundance of faint systems through a limit on cooling processes, molecular gas formation, or feedback (e.g., Sun & Furlanetto 2016). Additionally, given a large enough survey area to discover rare, bright galaxies, the abundance of objects at  $M_{\text{UV}} < -22$  can be determined. These luminous galaxies at  $z \gtrsim 6$  occur in an abundance larger than predicted by Schechter (1976) function fits, given the exponential cut-off at bright magnitudes. Instead, a double power-law (DPL) fit can be used with a functional form given by

$$y \equiv 10^{-0.4(M_{\text{UV}} - M_{\text{DPL}}^*)}, \quad 7.$$

$$\phi_{\text{DPL}}(M_{\text{UV}}) = 0.4 \ln 10 \phi_{\text{DPL}}^* [y^{-(\alpha+1)} + y^{-(\beta+1)}]^{-1}. \quad 8.$$

Here, the parameter  $\beta$  describes the power-law behavior brighter than the characteristic magnitude  $M_{\text{DPL}}^*$ . Fit to the same data, Equations 5 and 7 are not guaranteed to provide the same normalization or characteristic magnitude, and we denote the DPL parameters as  $\phi_{\text{DPL}}^*$  and  $M_{\text{DPL}}^*$  to distinguish them.

**Figure 3** shows determinations of the rest-frame UV luminosity function at redshifts  $z \sim 6, 7, 8, 9$ , and  $10$  collected from a small subset of the literature. The search for high-redshift galaxy populations and quantifying their  $\rho_{\text{UV}}$  evolution have been extensive undertakings by the community (e.g., Conselice et al. 2016, McLeod et al. 2016, Finkelstein et al. 2022). The data in **Figure 3** are by no means complete. The measurements in **Figure 3** include galaxies identified in both ground-based and HST imaging, using Lyman break drop-out selection techniques. The bright ends of the luminosity functions come from Harikane et al. (2022) at  $z \sim 6\text{--}7$  and Bowler et al. (2015, 2017, 2020) and Stefanon et al. (2019) at redshifts  $z \sim 8\text{--}9$ . At redshifts  $z \sim 6\text{--}9$ , most data fainter than  $M^*$  come from Bouwens et al. (2021a). At  $z \sim 10$ , the measurements by Oesch et al. (2018) are used, as updated by Bouwens et al. (2021a). Also shown are representative Schechter luminosity function models at  $z \sim 6\text{--}9$  from Bouwens et al. (2021a) and  $z \sim 10$  from Oesch et al. (2018), as well as DPL models from Harikane et al. (2022) at  $z \sim 6\text{--}7$  and from Bowler et al. (2020) at  $z \sim 8\text{--}9$ . The luminosity function model parameter values are reproduced in **Tables 1** and **2**.

The redshift-dependent luminosity functions provide an interesting picture for the evolution of galaxies in the cosmic reionization era. The overall abundance of galaxies brighter than  $M_{\text{UV}} \approx -16$  declines strongly from  $z \sim 6$  to  $z \sim 10$ . The luminosity function faint-end slope is steep, with  $\alpha \lesssim -2$ , but the degree of steepening with redshift depends on whether a Schechter or DPL model is used. The luminosity density  $\rho_{\text{UV}}$  ( $\text{erg s}^{-1} \text{ Hz}^{-1} \text{ Mpc}^{-3}$ ) can be computed by integrating the luminosity function weighted by galaxy luminosity. **Table 3** reports the luminosity density contributed by galaxies with luminosities  $L > 0.01L^*$ , for the luminosity function models shown in **Figure 3** with best-fit parameters provided in **Tables 1** and **2**. When put in the cosmological context, over the range of redshift  $z \sim 8\text{--}10$ , the luminosity density in the Universe

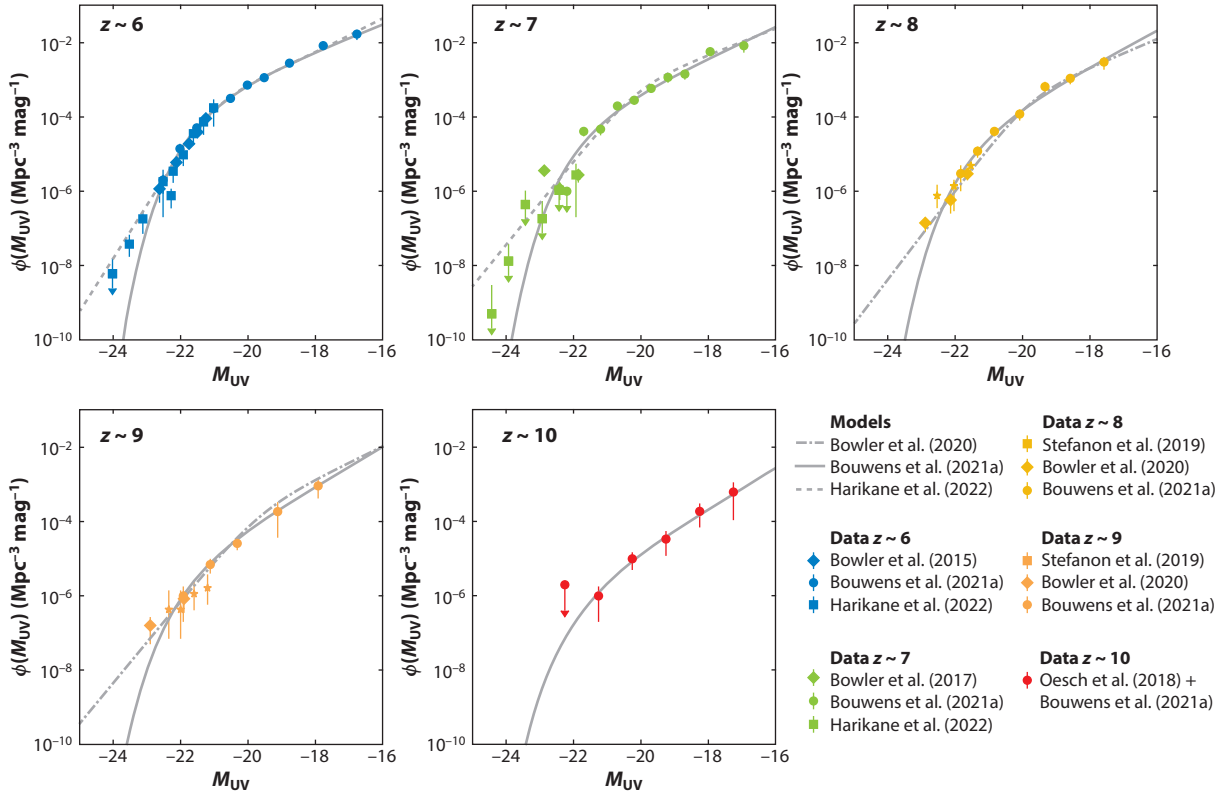


**Figure 3**

Rest-frame ultraviolet luminosity function of galaxies during cosmic reionization at redshifts  $z \approx 6$  (blue), 7 (green), 8 (yellow), 9 (orange), and 10 (red). Shown are data compiled from the most recent available literature at each magnitude, using both ground-based and *Hubble Space Telescope* observations to identify high-redshift galaxies based primarily on dropout color selections (Bowler et al. 2015, 2017, 2020; Oesch et al. 2018; Stefanon et al. 2019; Bouwens et al. 2021a; Harikane et al. 2022). Also shown are Schechter (1976) function (solid lines; Bouwens et al. 2021a) and double power-law (dotted and dashed lines; Bowler et al. 2020, Harikane et al. 2022) model fits that provide representations of the data with comparable quality. Empirically, the abundance of galaxies declines from  $z \sim 6$  to  $z \sim 10$ , with the faint-end slope steepening to  $\alpha < -2$  to roughly track the low-mass slope of the halo mass function. The Schechter function fits have characteristic magnitudes  $M^* \approx -21$  at all redshifts shown, whereas the pivot magnitude of the double power-law fits dims from  $M_*^{pl} \approx -21$  at  $z \sim 6$  to  $M_*^{pl} \approx -19.7$  at  $z \sim 9$ . Figure adapted from Bouwens et al. 2021a with permission.

changes by roughly an order of magnitude in less than 200 Myr. **Table 3** also reports the fractions of the luminosity densities at each redshift contributed by galaxies with luminosities  $L > 0.1L^*$  and  $L > L^*$ . The inferred relative importance of bright versus faint objects also depends on the luminosity function model used, reflecting the ability of the DPL model to capture the presence of

**Table 1** Schechter (1976) luminosity function  $\phi(M_{UV})$  parameters

Redshift	$\phi^* (\text{Mpc}^{-3} \text{ mag}^{-1})$	$M^* (\text{mag})$	$\alpha$	Reference
$z \sim 6$	$5.1^{+1.2}_{-1.0} \times 10^{-4}$	$-20.93 \pm 0.09$	$-1.93 \pm 0.08$	Bouwens et al. 2021a
$z \sim 7$	$1.9^{+0.8}_{-0.6} \times 10^{-4}$	$-21.15 \pm 0.13$	$-2.06 \pm 0.11$	Bouwens et al. 2021a
$z \sim 8$	$9^{+9}_{-5} \times 10^{-5}$	$-20.93 \pm 0.28$	$-2.23 \pm 0.20$	Bouwens et al. 2021a
$z \sim 9$	$2.1^{+1.4}_{-0.9} \times 10^{-5}$	$-21.15$ (fixed)	$-2.33 \pm 0.19$	Bouwens et al. 2021a
$z \sim 10$	$4.2^{+4.5}_{-2.2} \times 10^{-6}$	$-21.19$ (fixed)	$-2.38 \pm 0.28$	Oesch et al. 2018

**Table 2 Double power-law luminosity function  $\phi_{\text{DPL}}(M_{\text{UV}})$  parameters**

Redshift	$\phi_{\text{DPL}}^*(\text{Mpc}^{-3} \text{ mag}^{-1})$	$M_{\text{DPL}}^*(\text{mag})$	$\alpha$	$\beta$	Reference
$z \sim 6$	$3.02^{+0.70}_{-0.45} \times 10^{-4}$	$-21.03^{+0.09}_{-0.03}$	$-2.08^{+0.07}_{-0.06}$	$-4.57^{+0.09}_{-0.10}$	Harikane et al. 2022
$z \sim 7$	$8.91^{+2.31}_{-1.83} \times 10^{-4}$	$-20.12^{+0.12}_{-0.10}$	$-1.89^{+0.10}_{-0.09}$	$-3.81^{+0.10}_{-0.13}$	Harikane et al. 2022
$z \sim 8$	$4.83^{+2.25}_{-2.25} \times 10^{-4}$	$-19.80 \pm 0.26$	$-1.96 \pm 0.15$	$-3.98 \pm 0.14$	Bowler et al. 2020
$z \sim 9$	$2.85^{+1.39}_{-1.39} \times 10^{-4}$	$-19.67 \pm 0.33$	$-2.1$ (fixed)	$-3.75 \pm 0.22$	Bowler et al. 2020

extremely bright objects above the Schechter function exponential cut-off. Given the sharp drop of the Schechter model, even a small number of bright objects can provide number densities well in excess of the Schechter curve at  $M < M^*$ . The total luminosity densities between the Schechter and DPL model fits differ by factors of  $\approx 1.05$ –2, influenced by the differing contributions of bright galaxies. Galaxies brighter than  $L_*$  can provide roughly twice as large a relative contribution to  $\rho_{\text{UV}}$  in the DPL models compared with the Schechter fits. How these contributions translate to the relative importance of bright versus faint galaxies to cosmic reionization depends on the prior cosmic star-formation history and the variations in  $\xi_{\text{ion}}$  with galaxy luminosity and how the escape fraction  $f_{\text{esc}}$  may depend on other galaxy properties (e.g., Duncan & Conselice 2015; Sharma et al. 2016; Lewis et al. 2020; Naidu et al. 2020; Yung et al. 2020a,b). Indeed, in revisiting the relative contribution of bright galaxies to reionization Naidu et al. (2020) found that as much as  $\approx 45\%$  of the UV luminosity density at  $z \sim 7$  could be contributed by objects with  $M_{\text{UV}} < -20$ . Understanding the detailed process of cosmic reionization, including the expected redshift-dependent topology of ionized hydrogen, will require further constraints on the relative contribution of bright and faint galaxies over cosmic time. Forthcoming surveys with JWST, such as the wide-area COSMOS (Cosmic Evolution Survey)-Web program (see Section 8), should help resolve this question and could rebalance our views on the reionizing role of galaxies as a function of luminosity.

In noting the strong evolution in the luminosity density with redshift during cosmic reionization, the sense of whether  $\rho_{\text{UV}}$  is changing rapidly relative to expectations should be calibrated by theoretical models. By converting the observed  $\rho_{\text{UV}}$  to an SFR density  $\dot{\rho}_*$  using stellar population synthesis modeling, a comparison with predictions for the star formation in growing dark matter halos can be performed. For reference, the BPASS population synthesis models with binary stellar evolution (Eldridge et al. 2017; Stanway & Eldridge 2018, 2019) predict that a galaxy forming stars at a constant rate  $\psi = 1 \text{ M}_\odot \text{ year}^{-1}$  for 100 Myr will have a specific UV luminosity of  $\log_{10} L_{\text{UV}} \approx 28.1 \text{ erg s}^{-1} \text{ Hz}^{-1}$ . For a dust-free system this model then suggests an approximate conversion  $\log_{10} \dot{\rho}_* \approx \log_{10} \rho_{\text{UV}} - 28.1$ , which would yield  $\log_{10} \dot{\rho}_*(z \sim 10) \approx -3.3 (\text{M}_\odot \text{ year}^{-1} \text{ Mpc}^{-3})$ .

**Table 3 Luminosity density  $\rho_{\text{UV}}$**

Redshift	$\log_{10} \rho_{\text{UV}}^{\text{a}}$ ( $> 0.01L^*$ )	$\rho_{\text{UV}}(>L^*)/\rho_{\text{UV}}(>0.01L^*)$	$\rho_{\text{UV}}(>0.1L^*)/\rho_{\text{UV}}(>0.01L^*)$	$\log_{10} \rho_{\text{UV}}^{\text{DPL a}}$ ( $> 0.01L^*$ )	$\rho_{\text{UV}}^{\text{DPL}}(>L^*)/\rho_{\text{UV}}^{\text{DPL}}(>0.01L^*)$	$\rho_{\text{UV}}^{\text{DPL}}(>0.1L^*)/\rho_{\text{UV}}^{\text{DPL}}(>0.01L^*)$
$z \sim 6$	26.25 <sup>b</sup>	0.066	0.49	26.27	0.048	0.45
$z \sim 7$	26.05	0.046	0.42	26.20	0.106	0.57
$z \sim 8$	25.83	0.027	0.32	25.87	0.084	0.52
$z \sim 9$	25.41	0.019	0.28	25.72	0.068	0.44
$z \sim 10$	24.80	0.016	0.25	ND	ND	ND

<sup>a</sup>(erg s<sup>-1</sup> Hz<sup>-1</sup> Mpc<sup>-3</sup>).

<sup>b</sup>To convert  $\rho_{\text{UV}}$  to a star-formation rate density  $\dot{\rho}_*$  ( $\text{M}_\odot \text{ year}^{-1} \text{ Mpc}^{-3}$ ), a useful approximation is  $\log_{10} \dot{\rho}_* \approx \log_{10} \rho_{\text{UV}} - 28.1$ . This conversion assumes a 100-Myr-old, constant star-formation rate stellar population without dust (Eldridge et al. 2017).

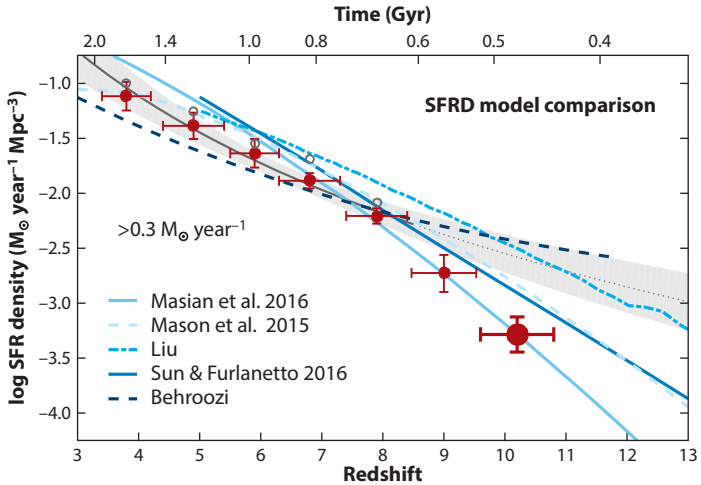


**Figure 4**

Evolution of the SFR density inferred from the evolving UV luminosity function. Shown are the SFR densities converted from integrating the UV luminosity function over a range of luminosities corresponding to a fixed minimum SFR  $> 0.3 \text{ M}_\odot \text{ year}^{-1}$  (red points with error bars). Empirically, the SFR density above this threshold evolves rapidly above  $z \sim 8$ . Also shown are some theoretical models for the SFR density evolution (blue lines; Mason et al. 2015, Mashian et al. 2016, Sun & Furlanetto 2016) and a power-law extrapolation fit to the  $z \leq 8$  data (gray area). Models with approximately redshift-independent star-formation efficiency with halo mass roughly track the redshift decline seen in the data (e.g., Mashian et al. 2016). Figure adapted from Oesch et al. (2018) with permission. Model results from Liu and Behroozi were provided by private communication to Oesch et al. Abbreviations: SFR, star-formation rate; SFRD, star-formation rate density.

**Figure 4** shows the evolving SFR determined by Oesch et al. (2018) at redshifts  $z \sim 4$ – $10$  from rest-frame UV-selected galaxies, along with theoretical models for  $\dot{\rho}_*(z)$  (Mason et al. 2015, Liu et al. 2016, Mashian et al. 2016, Sun & Furlanetto 2016). The best agreement between the theoretical models and the observed cosmic SFR history occurs for models in which the star-formation efficiency as a function of halo properties remains roughly constant with redshift. In these models the SFR density does decline rapidly with redshift in step with the abundance of dark matter halos, although the details of galaxy formation physics in the smallest halos can affect the normalization of the trends. Although not yet conclusive, a relatively sharp decline in both  $\rho_{\text{UV}}$  and  $\dot{\rho}_*$  above  $z \sim 8$  may therefore not be unexpected and may simply trace the evolution in halo abundance. Subsequent theoretical models of the high-redshift galaxy population reach similar conclusions about the connection between the redshift-constancy of the star-formation efficiency as a function of halo mass and the rapid decline in the SFR density (Mitra et al. 2015; Yue et al. 2016; Lapi et al. 2017; Yung et al. 2019a,b, 2020a,b; Behroozi et al. 2020), as do recent observational analyses (e.g., Bouwens et al. 2021a, Harikane et al. 2022).

## 2.7. Evolution of the Ionized Fraction

The volume fraction  $Q_{\text{HII}}(z)$  of ionized hydrogen in the IGM provides a convenient global summary of reionization. Below, we describe models for how  $Q_{\text{HII}}(z)$  evolves, which is subject to significant uncertainties beyond those associated with the production of IGM-ionizing radiation from galaxy populations already described in Sections 2.5 and 2.6. The detailed time dependence of the ionized fraction has not yet been measured. The Lyman- $\alpha$  (Ly $\alpha$ ) optical depth measured in the spectra of quasars suggests reionization must complete (e.g.,  $Q_{\text{HII}} > 0.9$ ) by  $z \sim 5.5$ – $6$  (Fan et al.

2006, McGreer et al. 2015, Boera et al. 2019). Other constraints have been determined, primarily through interpreting observations of Ly $\alpha$  emission or absorption at a variety of redshifts  $z \sim 6-8$ , finding  $Q_{\text{HII}} \sim 0.2-0.8$  (Davies et al. 2018; Mason et al. 2018, 2019; Hoag et al. 2019; Jung et al. 2020; Wang et al. 2020; Yang et al. 2020). Very recently, limits on the 21-cm power spectrum at  $z \sim 8$  and  $z \sim 10.4$  have been placed by the Hydrogen Epoch of Reionization Array (HERA; The HERA Collab. et al. 2021b). These limits can be combined with interpretative simulations to constrain the evolution of  $Q_{\text{HII}}(z)$  [The HERA Collab. et al. 2022a; see also Monsalve et al. 2017 for constraints from the EDGES [Experiment to Detect the Global EoR (Epoch of Reionization) Signature] experiment]. There are integral constraints on  $Q_{\text{HII}}$  from the electron scattering optical depth  $\tau$  to the cosmic microwave background (CMB).

Madau et al. (1999) provided a basic picture for the evolution of  $Q_{\text{HII}}(z)$  in the form of a differential equation for the time rate of change  $dQ_{\text{HII}}/dt$  arising from the competition between ionization and recombination. In its simplest form, the reionization equation can be written

$$\frac{dQ_{\text{HII}}}{dt} = \frac{\dot{n}_{\text{ion}}}{\langle n_{\text{H}} \rangle} - \frac{Q_{\text{HII}}}{\bar{t}_{\text{rec}}}, \quad 9.$$

where  $\langle n_{\text{H}} \rangle$  is the mean number density of hydrogen. The recombination time  $\bar{t}_{\text{rec}}$  is intended to capture possible variations in the recombination rate owing to density inhomogeneities, which is often represented (e.g., Madau et al. 1999) as

$$\bar{t}_{\text{rec}} = [(1 + Y/4X) * C \langle n_{\text{H}} \rangle \alpha(T)(1 + z)^3]^{-1}, \quad 10.$$

where  $Y$  is the helium abundance,  $X$  is the hydrogen abundance,  $\alpha$  is the temperature-dependent recombination coefficient of hydrogen (Case B, often taken at  $T = 20,000$  K), and the clumping factor is  $C \sim \langle n_{\text{H}}^2 \rangle / \langle n_{\text{H}} \rangle^2$ . Clumping factors of order  $C \lesssim 3$  at  $z \gtrsim 6$  are typically adopted, motivated by simulations (e.g., Finlator et al. 2012, Shull et al. 2012, Robertson et al. 2015, Gorce et al. 2018). Given the cosmological evolution of the mean density, the evolution of  $Q_{\text{HII}}$  is monotonic if  $\dot{n}_{\text{ion}}$  is monotonic. The observed evolution in  $\rho_{\text{UV}}$  (Section 2.6) makes this a reasonable assumption, although double reionization models are still being explored (Salvador-Solé et al. 2017). Once  $Q_{\text{HII}}$  is determined, the neutral fraction can be determined as  $x_{\text{H}_1} = 1 - Q_{\text{HII}}$ .

The simplified description of the evolution of the ionized fraction computed via Equation 9 is still in wide use for interpreting the impact of galaxy evolution on cosmic reionization (Finkelstein et al. 2019, Naidu et al. 2020). Given the complexity of the reionization process, the inadequacies of this model should not be surprising. Madau (2017) recently presented an augmentation of the reionization equation that accounts for the presence of dense, neutral absorbers after the IGM becomes mostly ionized through an additional opacity term, preventing the unphysical values of  $Q_{\text{HII}} > 0$ . Of course, full cosmological hydrodynamical simulations can be used to model the reionization, some of which include radiative transfer (see Section 3). In cosmological simulations, the photoionization rate is usually connected to a model for the evolving emissivity of galaxies (e.g., the  $\rho_{\text{UV}}$  in Table 3) and time-dependent mean free path of ionizing photons. The mean free path evolution may be assumed or computed directly via radiative transfer. However, most cosmological simulations adopt a fixed photoionization-rate history or adopt a single model for the ionizing input from stellar populations. Although Equation 9 allows for the convenient computation of  $x_{\text{H}_1}$  given a model for  $\dot{n}_{\text{ion}}$ , it does not track the physical impact of photoionization on the intergalactic gas including the photoheating associated with hydrogen and helium ionizations. The subsequent thermal and ionized fraction evolution of the IGM has a host of additional observational ramifications beyond the scope of this work (see the review by McQuinn 2016), so, in principle, the evolution of the neutral fraction during reionization and the properties of the IGM after reionization, such as the Ly $\alpha$  forest power spectrum, should be made

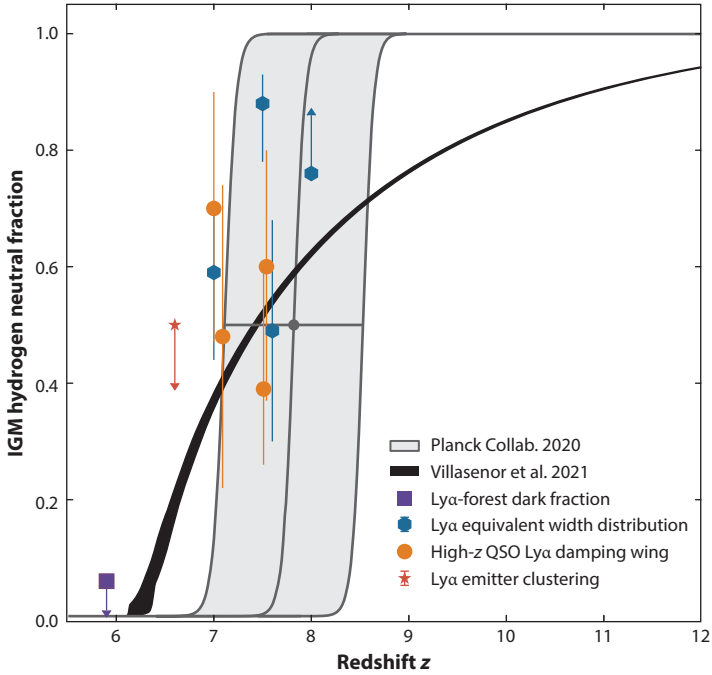


**Figure 5**

Constraints on the evolution of the hydrogen neutral fraction  $x_{\text{HI}}$  in the intergalactic medium. Most available constraints result from analyses of Ly $\alpha$  emission and absorption during cosmic reionization. From low redshift to high, constraints are inferred from the fraction of the Ly $\alpha$  and Lyman- $\beta$  forests that are dark (purple; McGreer et al. 2015), the clustering of Ly $\alpha$  emitters (red; Ouchi et al. 2010, Sobacchi & Mesinger 2015), the observed equivalent width distribution of  $z \sim 7$ –8 Ly $\alpha$  emitters (Mason et al. 2018, 2019; Hoag et al. 2019; Jung et al. 2020), and the Ly $\alpha$  damping wing of  $z \sim 7$ –8 quasars (Mortlock et al. 2011, Bañados et al. 2018, Davies et al. 2018, Wang et al. 2020, Yang et al. 2020). Leveraging the sensitivity of the CMB to the electron scattering optical depth, Planck Collab. et al. (2020) infers a midpoint of reionization of  $z(x_{\text{HI}} = 0.5) \sim 7.82 \pm 0.71$  (gray area, which reflects the Planck Collab. et al. 2020 tanh model for neutral fraction evolution). Also shown is a prediction from cosmological simulations for  $x_{\text{HI}}$  constrained by the evolution of the Ly $\alpha$  forest transmitted flux power spectrum at  $z < 6$ , allowing for variations in the range of photoionization and photoheating history (Villasenor et al. 2021). Abbreviations: CMB, cosmic microwave background; IGM, intergalactic medium; Ly $\alpha$ , Lyman- $\alpha$ ; QSO, quasistellar object.

consistent. Villasenor et al. (2021) used hundreds of hydrodynamical cosmological simulations, varying the amplitude and timing of the Puchwein et al. (2019) photoionization and photoheating rates, and determined a photoionization and photoheating history that matches all the available data on the Ly $\alpha$  forest at  $z < 5$ . These fits then provide a prediction for the neutral fraction evolution  $x_{\text{HI}}(z)$  that is fully consistent with the postreionization properties of the IGM. Note this model, like Puchwein et al. (2019), assumes  $f_{\text{esc}} \approx 0.18$  during reionization, but the amplitude and timing of the photoionizing background are allowed to vary.

We plot several types of observational constraints on  $x_{\text{HI}}(z)$  and the model by Villasenor et al. (2021) in **Figure 5**. McGreer et al. (2015) quantified the neutral fraction near the end of reionization using dark regions of the Ly $\alpha$  and Ly $\beta$  forests in background quasar spectra that transmit zero flux. At  $z = 5.9$ , this measurement provides  $x_{\text{HI}} \leq 0.06 \pm 0.05$  as is shown as an upper limit in **Figure 5**. The clustering of Ly $\alpha$  emitters limits  $x_{\text{HI}} < 0.5$  at  $z = 6.6$  (Ouchi et al. 2010, Sobacchi & Mesinger 2015). The equivalent width distribution of Ly $\alpha$  emitters at  $z \sim 7$ –8 also constrains

the neutral fraction of the IGM to be  $x_{\text{H}_1} = (0.59^{+0.11}_{-0.15}, 0.88^{+0.05}_{-0.10}, 0.49 \pm 0.19, >0.88)$  at  $z = (7, 7.5, 7.6, 8)$ , respectively (Mason et al. 2018, 2019; Hoag et al. 2019; Jung et al. 2020). The Ly $\alpha$  damping wing in the spectra of high-redshift quasars indicates the neutrality of the surrounding IGM, as shown by Davies et al. (2018). Four high- $z$  quasars have damping wing constraints that give  $x_{\text{H}_1} = (0.70^{+0.20}_{-0.23}, 0.48^{+0.26}_{-0.26}, 0.60^{+0.20}_{-0.23}, 0.39^{+0.22}_{-0.13})$  at  $z = (7.00, 7.09, 7.54, 7.51)$  (Mortlock et al. 2011, Bañados et al. 2018, Wang et al. 2020, Yang et al. 2020). Also shown is the constraint from Planck Collab. et al. (2020) on the midpoint of reionization  $z(x_{\text{H}_1} = 0.5) \sim 7.82 \pm 0.71$ , which assumes a tanh model for  $x_{\text{H}_1}(z)$  and is therefore not independent of the assumed reionization history. The Villaseñor et al. (2021) model is shown for reference, noting that the model is not fit to the data shown in **Figure 5**. Overall, there is general consistency between the data and the cosmological model, but the relative agreement highlights that more and significantly tighter constraints would be helpful in discriminating between different models of the reionization history.

The CMB observations by Planck Collab. et al. (2020) provide an additional constraint on the reionization history. The optical depth  $\tau$  of electron scattering measured by CMB experiments involves an integral over  $Q_{\text{HII}}(z)$  as

$$\tau(z) = c \langle n_{\text{H}} \rangle \sigma_{\text{T}} \int_0^z f_e Q_{\text{HII}}(z') H^{-1}(z') (1+z')^2 dz', \quad 11.$$

where  $c$  is the speed of light,  $n_{\text{H}}$  is the comoving hydrogen density,  $\sigma_{\text{T}}$  is the Thomson cross section,  $H(z)$  is the Hubble parameter as a function of redshift  $z$ , and  $f_e$  is the number of free electrons per hydrogen nucleus, which also depends on the ionization state of helium. The *Planck* satellite measured a value  $\tau = 0.0561 \pm 0.0071$  with 68% confidence when constrained by the CMB and low-redshift baryon acoustic oscillations (Planck Collab. et al. 2020). At redshifts in which intergalactic hydrogen is fully ionized (a constant  $Q_{\text{HII}} = 1$ ), Equation 1 increases owing to the matter-dominated behavior of  $H(z)$  and the  $(1+z)^2$  weighting of the integrand. Once  $Q_{\text{HII}}$  drops to  $Q_{\text{HII}} < 1$ , the increase of  $\tau$  with redshift moderates. For a redshift-independent  $f_{\text{esc}}$  and  $\xi_{\text{ion}}$ , there is a correspondence between the Thomson optical depth  $\tau$  and the SFR density  $\dot{\rho}_{\star}$  (Robertson et al. 2015). For models that match the neutral fraction evolution shown in **Figure 5**, the constraint from  $\tau$  mostly then relates to the persistence of the global cosmic star-formation history at very high redshifts ( $z > 8$ ).

### 3. MODELS OF HIGH-REDSHIFT GALAXY FORMATION AND REIONIZATION

Simulations of galaxy formation during cosmic reionization and its possible connection to the evolution of the IGM have advanced substantially in recent years. The inclusion of radiative transfer (including postprocessing) or radiation hydrodynamics allow for an understanding of how galaxies produce hydrogen-ionizing photons, how those photons escape to the IGM, and the bulk effects of the star-forming population on the reionization process. Below, we review some recent efforts to model the galaxy population before and during reionization, including simulations that make specific predictions for observations with JWST. Zoom-in cosmological simulations with radiative transfer provide means for understanding the physical origin of the escape fraction (e.g., Ma et al. 2016, 2020; Barrow et al. 2020; Secunda et al. 2020; Mauerhofer et al. 2021), and these are discussed further in Section 2.2.

Simulations with radiative transfer provide a detailed physical description of cosmic reionization that the framework presented in Section 2 can only coarsely approximate. These simulations can track the reionization process from early times through its completion and quantify the relative contribution of faint and bright galaxies to the ionization budget (e.g., Gnedin 2014, Gnedin & Kaurov 2014, Xu et al. 2016, Lewis et al. 2020, Lovell et al. 2021). Simulations also predict

how the distributions of galaxy metallicities and ages influence the mass-dependent contribution of ionizing photons to the reionization process (e.g., Katz et al. 2018). The detailed calculations can follow the histories of individual galaxies, allowing researchers to study how the reionization process affects regions around galaxies as a function of halo mass (Zhu et al. 2019).

Several recent studies have made predictions for the photometric properties of high-redshift galaxies from cosmological simulations. In general, the simulations roughly match the observed UV luminosity functions (O’Shea et al. 2015, Gnedin 2016, Wilkins et al. 2017, Vogelsberger et al. 2020, Vijayan et al. 2021). Interestingly, despite the observed blue UV continua of high-redshift galaxies, some models predict substantial obscured star formation even at high redshift (Vijayan et al. 2021). Simulations can be used to predict the LyC leakage and nebular emission in high-redshift galaxies, enabling the interpretation of future JWST spectra (e.g., Zackrisson et al. 2017). Simulations are complemented by semianalytical models, which have predicted the feedback of the reionization process on galaxy formation (Bose et al. 2018), studied the role of AGNs in reionization (Khaire et al. 2016, Dayal et al. 2020), and quantified the effects of cosmic variance in studies of distant galaxies with JWST (Ucci et al. 2021).

Forthcoming observations with JWST will provide critical tests of these models. Detailed calculations compute the redshift-dependent SFR and stellar mass content of galaxies, and until JWST only the very brightest galaxies in the cosmic reionization era have had stellar mass inferences enabled by *Spitzer* to compare with model predictions (see Section 6). By extending the stellar mass constraints to much lower galaxy masses, JWST will determine whether both the instantaneous rate and time-integrated history of star formation in the earliest galaxies are reliably predicted by existing theoretical approaches. Correspondingly, the model predictions for how stellar mass and star formation relate to dark matter halo properties can be tested by JWST. The comparisons between theory and observation will enable an assessment of our understanding of the physics of dark matter structure formation, cooling, and feedback processes in the first billion years of cosmic history.

#### 4. ROLE OF ACTIVE GALACTIC NUCLEI AND QUASARS

AGNs represent a potentially important source of ionizing radiation. Their relative rarity and the difficulty in definitively distinguishing them from galaxies using static, broadband photometry make quantifying the role of AGNs in the cosmic reionization process challenging. An assessment of the contribution of AGNs to cosmic reionization requires reviewing important results over the past  $\sim 5$  years, which have in total led to the current near-consensus that AGNs are a subdominant source of hydrogen ionizing photons during the reionization era. Nonetheless, high-redshift quasars can provide critical probes of the IGM neutrality during cosmic reionization.

Giallongo et al. (2015) identified faint AGN candidates in HST/CANDELS (Cosmic Assembly Near-infrared Deep Extragalactic Legacy Survey) GOODS-S imaging, leading to estimates of enhanced numbers of low-luminosity AGNs to the hydrogen ionizing budget at high redshift. Madau & Haardt (2015) carefully considered the implications of these potential AGNs on reionization and concluded that if a large number of faint AGNs existed at  $z \sim 6$  they could potentially provide enough LyC radiation to reionize the Universe without a substantial contribution from galaxies. The escape fraction of ionizing photons from AGNs should be substantially enhanced relative to galaxies, with estimates at  $z \sim 3\text{--}4$  of  $\approx 75\%$  (Grazian et al. 2018) and, even with their relative rarity compared with galaxies, faint AGNs would be efficient agents of reionization (e.g., Khaire et al. 2016).

Later studies of potential AGN contributions to reionization drew more conservative conclusions about their role. If AGNs did contribute most of the high-redshift LyC, it would lead to

large variations in the hydrogen Ly $\alpha$  forest during the end of cosmic reionization, impact the mean opacity of the HeII Ly $\alpha$  forest, and lead to substantial photoheating of the IGM through early HeII reionization (D'Aloisio et al. 2017). Parsa et al. (2018) reported that many potential faint AGNs in HST images were unconvincing and, given candidates they found reliable, that AGNs failed by a factor of roughly an order of magnitude at redshift  $z \sim 6$  to solely reionize intergalactic hydrogen. Subaru searches for bright quasars at  $5.7 \lesssim z \lesssim 6.5$  (Matsuoka et al. 2016) produced AGN luminosity functions that likely would only support 10% of the required ionizing photon budget at the end of reionization (Matsuoka et al. 2018). Recent determinations of the high-redshift AGN luminosity function agree that at  $z \sim 6$  AGNs are subdominant (about a few percent; Kulkarni et al. 2019), and current uncertainties in the faint end of the high-redshift bolometric luminosity are unlikely to change this conclusion (Shen et al. 2020). Given the current observed AGN luminosity functions, most theoretical models that can reproduce them conclude that AGNs do not drive reionization (e.g., Hassan et al. 2018, Mitra et al. 2018) but that AGNs can dominate the LyC production among the galaxy population at the highest stellar masses (Dayal et al. 2020).

Some of our most critical information on the ionization state of the IGM is inferred from the spectra of highest-redshift quasars. Mortlock et al. (2011) discovered the first quasar at  $z > 7$  in the UKIDSS (U.K. Infrared Deep Sky Survey) Large Area Survey (ULAS), with redshift  $z = 7.085$ . This discovery has been followed by several others at  $z \approx 7.0\text{--}7.642$  identified by a combination of ULAS, Dark Energy Survey, *Wide-Field Infrared Survey Explorer*, United Kingdom Infrared Telescope, and Subaru observations (Bañados et al. 2018; Yang et al. 2019, 2020; Wang et al. 2020; Izumi et al. 2021; Wang et al. 2021), as well as interesting quasi-stellar objects at just slightly lower redshifts (e.g., Wang et al. 2019). Davies et al. (2018) used the Ly $\alpha$  damping wing profile in the spectra of the quasars discovered by Mortlock et al. (2011) and Bañados et al. (2018) to place constraints on the neutral fraction of the IGM at  $z = 7.085$  ( $x_{\text{H}_1} = 0.48^{+0.26}_{-0.26}$ ) and  $z = 7.54$  ( $x_{\text{H}_1} = 0.60^{+0.20}_{-0.23}$ ), respectively. Two additional quasars have had Ly $\alpha$  damping wing measurements of their local IGM neutral fraction at  $z = 7.00$  ( $x_{\text{H}_1} = 0.70^{+0.20}_{-0.23}$ ; Wang et al. 2020) and  $z = 7.515$  ( $x_{\text{H}_1} = 0.39^{+0.22}_{-0.13}$ ; Yang et al. 2020). These four measurements are discussed in the context of the evolving neutral fraction in Section 2.7. Unfortunately, the high-redshift quasar at  $z \sim 7.642$  discovered by Wang et al. (2021) cannot currently provide a reliable Ly $\alpha$  damping wing measurement owing to complications from SiIV broad absorption lines.

Combined observations of AGNs and galaxies can also provide insight into cosmic reionization. Quasars create ionized proximity zones, and the study of galaxies in the proximity zones can inform us about the end of the reionization process (Bosman et al. 2020). Along the line of sight to high-redshift quasars, the correlation between IGM transmission and the presence of galaxies near the sightline can enable estimates of the high-redshift galaxies' LyC escape fractions (Kakiuchi et al. 2018), which provide  $f_{\text{esc}} = 0.14^{+0.28}_{-0.05}$  (Meyer et al. 2020; see also Section 2.2).

## 5. INNOVATIONS IN HIGH-REDSHIFT GALAXY OBSERVATIONS

The pursuit of high-redshift galaxies during cosmic reionization has involved primarily the combination of deep multiband imaging with drop-out selections and follow-up spectroscopy in contiguous fields chosen for their accessibility, reddening, and some sense of how typical they might be for regions of the distant Universe. Over the past decade, significant innovations in the search for high-redshift galaxies have been made and some are described below. These innovations should not be seen as somehow separate from the standard approach, and indeed the results from these observations are integrated in the discussion elsewhere in this review (especially in Section 2.6).

Nonetheless, they warrant particular note as each innovation has relevance for future studies of the high-redshift Universe with JWST.

### 5.1. Gravitationally Lensed Observations

The use of gravitational lenses to magnify faint objects has become increasingly widespread in galaxy surveys. Significant investment by HST through the Frontier Fields program (Lotz et al. 2017) has now provided deep multiband images of several strong-lensing clusters of galaxies (Abell 2744, MACSJ0416.1-2403, MACSJ0717.5+3745, MACSJ1149.5+2223, Abell S1063, and Abell 370). The Frontier Fields complemented the predecessor Cluster Lensing and Supernova Survey with Hubble (CLASH) imaging survey (Postman et al. 2012) and the Grism Lens-Amplified Survey from Space (GLASS; Treu et al. 2015) that provided HST IR grism observations of the Frontier Fields and four additional clusters. Although the Frontier Fields focused on deep imaging of select clusters and parallel “blank” fields, the Reionization Lensing Cluster Survey (RELICS; Coe et al. 2019) targeted a larger number (41) of clusters with shallower imaging. The cluster observations by the Frontier Fields, CLASH, GLASS, and RELICS can probe to substantially fainter luminosities at fixed integration time than blank field observations that do not benefit from the aid of gravitational lensing. However, this increased power is balanced against the added complexity of modeling the gravitational lens systems to understand the magnification map of the foreground (e.g., Meneghetti et al. 2017) and by the decreased volume probed at high-magnification relative to a blank field at the same intrinsic depth that leads to higher cosmic variance uncertainty (Robertson et al. 2014).

Gravitational lensing clusters have been particularly useful for identifying distant dropout galaxies (e.g., Zheng et al. 2012, 2017; Salmon et al. 2018, 2020) investigating the faint-end slope of the galaxy luminosity function during cosmic reionization (Atek et al. 2015; McLeod et al. 2015, 2016; Bouwens et al. 2017; Livermore et al. 2017; Ishigaki et al. 2018; Kawamata et al. 2018; Yue et al. 2018; Bhatawdekar et al. 2019; Furtak et al. 2021). Lensing clusters have also been helpful in amplifying signals for reionization-era observations that are less efficient than HST broadband imaging, including *Spitzer*/IRAC (Infrared Array Camera; Shipley et al. 2018, Kikuchi et al. 2020, Strait et al. 2020), slit and grism spectroscopy (e.g., Schmidt et al. 2016, Mason et al. 2019, Fuller et al. 2020, Pelliccia et al. 2020), and intermediate band imaging (Hernán-Caballero et al. 2017). The results of many of these efforts have been incorporated into the analyses that arrive at the luminosity functions reported in Section 2.6 (e.g., Bouwens et al. 2021a).

### 5.2. Pure-Parallel Surveys

The ability with HST and with the forthcoming JWST to integrate with two instruments simultaneously provides an extreme advance in observational efficiency. Pure-parallel surveys enable extremely wide areas to be covered essentially for free while prime focus surveys are being conducted, allowing for survey volumes that exceed traditional contiguous campaigns at the expense of some added complexity of analysis and nonuniformity in the depths and coverage. Two important HST parallel imaging surveys include the Brightest of Reionizing Galaxies (BoRG) Survey (Trenti et al. 2011) and the Hubble Infrared Pure Parallel Imaging Extragalactic Survey (HIPPIES; Yan et al. 2011).

Pure-parallel imaging provides some of the best constraints on rare, luminous high-redshift galaxies (Bradley et al. 2012; Schmidt et al. 2014; Calvi et al. 2016; Morishita et al. 2018, 2020; Bridge et al. 2019; Rojas-Ruiz et al. 2020; Morishita 2021). In discovering luminous objects, these surveys also provide candidate high-redshift galaxies detected in parallel grism observations (Bagley et al. 2017) or that can be targeted spectroscopically to help determine the reliability of drop-out selections (Livermore et al. 2018).

### 5.3. ALMA Observations of High-Redshift Galaxies

A remarkable advance in the study of cosmic reionization has been the ability to detect and interpret properties of gas and dust in distant galaxies. With exquisite sensitivity, ALMA can reveal continuum and spectroscopic signatures deep into the reionization era that have been unobtainable in the past. These observations complement the photometry and spectroscopy from HST, ground-based large telescopes, and JWST that remain limited to much shorter wavelengths than what ALMA can achieve.

In addition to the critical ALMA imaging of the Hubble Ultra Deep Field (HUDF; Dunlop et al. 2017), spectroscopic surveys of the HUDF and other deep fields have been conducted with ALMA (Hodge et al. 2013, Walter et al. 2016, Franco et al. 2018). ALMA spectroscopy allows for the detection of highly redshifted [OIII] 88- $\mu\text{m}$  (e.g., Inoue et al. 2016) and [CII] 158- $\mu\text{m}$  (e.g., Maiolino et al. 2015) lines during cosmic reionization, and directly probes coolants in the ISM of distant galaxies. The spectroscopic confirmation of the highest-redshift galaxies with ALMA, especially with [OIII] (e.g., Hashimoto et al. 2018), is discussed in Section 7.1. The longer-wavelength [CII] line is now often used to study  $z \sim 7$  galaxies (Pentericci et al. 2016, Bradač et al. 2017, Carniani et al. 2017). Ongoing large programs with ALMA will study many bright blank field galaxies in both [CII] and [OIII] (Bouwens et al. 2021b). The high resolution of ALMA allows for the investigation of spatial offsets between Ly $\alpha$  and [CII] emission (Maiolino et al. 2015) at redshifts  $z > 7$ , providing new information on the interior structure of high-redshift galaxies. ALMA continuum measurements also provide evidence of dust in at least some  $z > 7$  objects in abundances not uncommon for present-day galaxies (Watson et al. 2015, Laporte et al. 2017; see Casey et al. 2014 for a broader review of dust in high-redshift galaxies). Comparisons between observational and theoretical studies of the connection between [CII] emission and star formation during cosmic reionization will provide insight into the evolving stellar radiation fields and conditions inside these early-forming galaxies (Lagache et al. 2018).

## 6. HIGH-REDSHIFT GALAXY STELLAR MASS CONSTRAINTS

The stellar mass content of high-redshift galaxies remains an area with great promise for future study, especially with JWST. To date, the best constraints on the stellar mass of high-redshift galaxies come from combinations of *Spitzer* IRAC 3.6- $\mu\text{m}$  and 4.5- $\mu\text{m}$  observations with HST or ALMA data. For a summary of *Spitzer* results at  $z > 4$ , see the recent review by Bradač (2020).

Once the HUDF, CANDELS, and CLASH survey data had been completed and augmented by *Spitzer* data (e.g., Bradač et al. 2014, Labbé et al. 2015), combining *Spitzer* with HST/WFC3-IR enabled the first constraints on the stellar mass function evolution to redshift  $z \sim 7$  (Stark et al. 2013, Duncan et al. 2014, Grazian et al. 2015). These studies found that the high-redshift stellar mass function steepened considerably to  $z \sim 7$  (see also Davidzon et al. 2017). By redshift  $z \sim 8$  the stellar mass function reaches  $\alpha < -2$ , but with large uncertainties (Song et al. 2016a). Similar conclusions were drawn by converting the rest-frame optical luminosity function to  $z \sim 7$  to a stellar mass function (Stefanon et al. 2017) and by using initial observations of the Frontier Fields to extend this observed steepening to  $z \sim 9$  (Bhatawdekar et al. 2019). Subsequently, Kikuchihara et al. (2020) have claimed based on more complete Frontier Fields data that  $\alpha \approx -1.8$ , perhaps moderating the abundance of low stellar mass objects during cosmic reionization. Recently, with expanded *Spitzer* imaging of the GOODS fields, Stefanon et al. (2021) have been able to constrain the stellar mass of objects to  $10^8 M_\odot$  with  $\approx 70\%$  completeness. They find stellar mass functions to  $z \sim 10$  to be consistent with a steep faint-end slope  $\alpha \approx -2$ , and that though the stellar mass in galaxies increases by  $\sim 1,000$  times over the redshift range  $z \sim 6-10$  the stellar-mass to halo-mass ( $M_\star - M_h$ ) ratios of galaxies do not substantially change. Stellar mass and halo mass appear to

be growing jointly apace during cosmic reionization, instilling the  $M_{\star} - M_h$  relation observed at lower redshifts (for a review, see Wechsler & Tinker 2018).

Despite this progress, the role for JWST will be substantial. A key theme in the interpretation of stellar mass observations is the possible role of nebular emission contamination of the rest-frame optical data probed by *Spitzer* (e.g., Stark et al. 2013, Smit et al. 2014). Owing to the strong nebular lines powered by reprocessing of internal LyC radiation, galaxies can display boosted broadband measures of their rest-frame optical emission beyond the continuum level supplied by evolved stars. Depending on the redshift and line strength, as strong lines pass through the *Spitzer* bands the rest-frame optical broadband colors of the object may change (e.g., Roberts-Borsani et al. 2016). Without spectroscopic redshifts, a wide range of stellar masses can be inferred from *Spitzer* IRAC observations of even bright  $z \sim 8$  candidate galaxies (Strait et al. 2020). JWST will provide rest-frame optical spectroscopy to  $\lambda \approx 5 \mu\text{m}$  with NIRSpec (Near Infrared Spectrograph) at depths sensitive enough to reach [OIII]+H $\beta$  in  $z \sim 8$ -9 galaxies, and can disentangle the possible contribution of nebular emission and evolved stellar populations to the rest-frame optical broadband flux observed.

Although the ultimate resolution to this issue may be rest-frame optical spectroscopic observations with JWST to  $z \sim 9$ , in the near term spectroscopic redshift confirmation with ALMA provides a significant benefit in the stellar mass solution of high-redshift objects (Roberts-Borsani et al. 2020). Observations of the gravitationally lensed galaxy MACS1149-JD, originally identified in CLASH by Zheng et al. (2012), with ALMA revealed 88  $\mu\text{m}$  [OIII] at  $z = 9.1096$  (Hashimoto et al. 2018). This redshift confirmation enabled the stellar population synthesis models to infer confidently the presence of evolved stellar mass in this distant object, pointing to star formation commencing as early as redshift  $z \sim 15$ . Without the spectroscopic redshift, the possibility of nebular contamination would make the stellar mass inference less certain. Ground-based Ly $\alpha$  redshifts can still provide a similar benefit in firming up the stellar population inferences on  $z \sim 9$  galaxies, which has allowed Laporte et al. (2021b) to determine that in  $z \gtrsim 9$  galaxies about 70% of their stellar mass may be in place before  $z \sim 10$ . Regardless of the current facility enabling the observation, depending on the exact redshift, in some cases it may not be possible to rule out nebular contamination given pre-JWST data.

## 7. SPECTROSCOPY OF THE HIGHEST-REDSHIFT GALAXIES

Spectroscopy enables us to understand the astrophysical principles that give rise to the observable properties of the galaxy population. Although we can learn much from the photometric properties of galaxies alone, the detailed wavelength-dependent flux information that is available from spectra allows us to more closely connect observations with atomic and nebular physics. For the distant Universe, JWST will measure rest-frame optical spectra that contain rich physical information on the detailed properties of galaxies. JWST will also enable the routine spectroscopic confirmation of photometric candidate sources at extreme distances. Below, we review some of the current status of redshift confirmation and spectroscopic astrophysics for distant galaxies. Anticipated advances with JWST in these areas will be discussed in Section 8.

### 7.1. Spectroscopic Confirmation of Distant Galaxy Redshifts

The large majority of the galaxies contributing to determinations of the evolving luminosity density are photometric detections only, with substantial uncertainty in their redshifts. The capabilities of facilities like the Keck Observatory, the VLT, and the Magellan Telescopes to provide deep, near-IR spectroscopy from the ground and HST to enable slitless IR spectroscopy without contamination by the sky have substantially advanced our understanding of the high-redshift Universe

by observing Ly $\alpha$  ( $\lambda = 1216 \text{ \AA}$ ), Nv ( $\lambda = 1243 \text{ \AA}$ ), CIV ( $\lambda = 1548, 1550 \text{ \AA}$ ), OIII] ( $\lambda = 1666 \text{ \AA}$ ), and CIII] ( $\lambda = 1907, 1909 \text{ \AA}$ ) emission lines at  $z > 7$ . Now, combined with the powerful ability of the ALMA to detect redshifted [OIII] ( $\lambda = 88 \mu\text{m}$ ) and [CII] ( $\lambda = 157 \mu\text{m}$ ), spectroscopic observations of galaxies at  $z > 7$  have become increasingly reliable and informative.

Redshifted Ly $\alpha$  remains a mainstay for high-redshift spectroscopic confirmations. A small population of galaxies with redshifts  $7.5 \gtrsim z \gtrsim 8$  have been confirmed, often selected from HST CANDELS imaging. These include an early discovery of Ly $\alpha$  emission at  $z = 7.51$  (Finkelstein et al. 2013), which also has a grism continuum measurement of the Lyman break (Tilvi et al. 2016). Over the next few years, this object was followed by a range of Ly $\alpha$  emitters spectroscopically confirmed at  $z = 7.45-8$  (Oesch et al. 2015, Roberts-Borsani et al. 2016, Song et al. 2016b, Hoag et al. 2017, Stark et al. 2017, Larson et al. 2018, Jung et al. 2019), including a gamma-ray burst host galaxy at  $z = 7.8$  (Tanvir et al. 2018) and a primitive galaxy group at  $z = 7.7$  (Tilvi et al. 2020). Recently, a large-scale campaign with Keck/MOSFIRE using 10 nights targeted six dozen systems, achieving 10 detections at redshifts  $z = 7.1-8.2$  (Jung et al. 2020; see also Pentericci et al. 2018). The demonstrated ability to spectroscopically confirm high-redshift galaxies using near-UV emission lines redward of Ly $\alpha$  was a hallmark achievement for the study of early galaxies. As discussed in Section 2.7, the presence of neutral hydrogen in the IGM during the cosmic reionization process can substantially attenuate Ly $\alpha$ . Having other available lines for spectroscopic redshift confirmation may therefore be critical during the reionization process and at earlier times. Stark et al. (2015a) detected CIII] 1909  $\text{\AA}$  in galaxies at  $z \sim 6.029$  and  $z = 7.213$  with known Ly $\alpha$  redshifts. Stark et al. (2015b) detected CIV 1243  $\text{\AA}$  in a galaxy with known Ly $\alpha$  redshift of  $z = 7.045$ . Laporte et al. (2017) detected Ly $\alpha$  and CIII] in a  $z \sim 6.8$  galaxy. At slightly lower redshift, an interesting discovery for understanding the internal ionizing spectrum of star-forming galaxies was the confirmation of CIV 1550  $\text{\AA}$  and OIII]  $\lambda = 1666 \text{ \AA}$  in a galaxy with known Ly $\alpha$   $z = 6.11$  (Mainali et al. 2017). The presence of CIII] has now been confirmed in galaxies at  $z = 7.51$  (Hutchison et al. 2019; same object as Finkelstein et al. 2013),  $z = 7.73$  (Stark et al. 2017; same object as Oesch et al. 2015), and recently  $z = 7.945$  (Topping et al. 2021).

Confirming spectroscopically the redshifts of the most distant candidates proves especially useful. Given the rapid apparent decline in the UV luminosity density  $\rho_{\text{UV}}$  in photometrically selected candidates  $z > 8$ , any confirmed redshifts further establish what galaxy population is reliably known to exist at these early times. Extremely distant objects have been confirmed via Ly $\alpha$  and Nv 1243  $\text{\AA}$  emission at redshift  $z = 8.68$  (Zitrin et al. 2015, Mainali et al. 2018), and with Ly $\alpha$  and ALMA [OIII] 88  $\mu\text{m}$  at  $z \sim 8.38$  (Laporte et al. 2017).

The object MACS0416-Y1 identified in the HST Frontier Fields (Zheng et al. 2012) was spectroscopically confirmed at  $z = 8.312$  with ALMA detections of [OIII], [CII], and dust emission (Tamura et al. 2019, Bakx et al. 2020). Using Keck and VLT, Laporte et al. (2021a) confirmed Ly $\alpha$  redshifts of  $z = 8.78$  for GN-z-10-3 and (tentatively)  $z = 9.28$  for MACS0416-JD. The candidate MACS1149-JD1 was confirmed to lie at  $z = 9.1096$  using ALMA [OIII] 88  $\mu\text{m}$  (Hashimoto et al. 2018). Interestingly, in the  $z = 8.38$  and  $z = 9.1$  [OIII] 88- $\mu\text{m}$  emitters, [CII] 158  $\mu\text{m}$  has not yet been detected (Laporte et al. 2019). Some objects at lower redshifts ( $z = 7.15$ ) have simultaneous ALMA [OIII] 88- $\mu\text{m}$ , [CII] 158- $\mu\text{m}$ , and dust continuum detections (Hashimoto et al. 2019).

The most distant known, spectroscopically confirmed object is the GOODS-N galaxy GN-z11 originally identified using HST WFC3/IR imaging. Oesch et al. (2016) used HST grism spectroscopy to measure a continuum spectral break for GN-z11 corresponding to redshift  $z = 11.09^{+0.08}_{-0.12}$ . Recently, using the Keck/MOSFIRE, Jiang et al. (2021) confirmed the redshift using three rest-frame UV emission lines, finding a redshift of  $z = 10.957$  if the lines correspond to the CIII] doublet and OIII].

## 7.2. Spectroscopic Probes of Reionization-Era Galaxy Astrophysics

Beyond the utility of redshift confirmation for distant objects, spectra contain vital information on the astrophysics of early galaxies. Given the current limitations on obtaining rest-frame optical spectra of distant galaxies before JWST, most spectroscopy at  $z \gtrsim 3$  is limited to rest-frame UV. The Ly $\alpha$  emission line itself provides rich astrophysical information, but we defer to the recent review by Ouchi et al. (2020) on Ly $\alpha$  emitters and their properties. Below, we touch briefly on the use of other lines as potential astrophysical probes of high-redshift galaxies.

Given their current accessibility via ground-based spectroscopy, UV emission lines are of particular interest today. Jaskot & Ravindranath (2016) used photoionization models to show that CIII] is expected to be the second brightest emission line (next to Ly $\alpha$ ) in high-redshift galaxies blueward of  $\lambda \sim 2700$  Å in the rest frame. Stark et al. (2015a, 2017) have connected the detection of CIII] in  $z > 7$  galaxies to enhanced internal ionization fields. Not all high-redshift Ly $\alpha$  lines display bright UV metal lines or show evidence for Nv 1243 Å that may indicate an AGN contribution or strongly shocked ISM gas (Mainali et al. 2018).

Once JWST NIRSpec provides the ability to expose deeper and redder spectra than currently possible, a host of additional probes of high-redshift galaxies will become available. At redshifts  $z \sim 5$  and  $z \sim 6$ , the mean rest-UV spectra of star-forming galaxies show evidence for enhanced photon production rates relative to local galaxies (Harikane et al. 2020, Pahl et al. 2020). The presence of strong [OIII]+H $\beta$  emission in high-redshift galaxies inferred from *Spitzer* photometry and colors will provide additional information. High-redshift objects with strong inferred [OIII] equivalent widths show abundant Ly $\alpha$  emission, suggesting a strong radiation field (Endsley et al. 2021a,b). The [OIII] emission itself requires efficient ionizing photon production, and photometric measures of OIII+H $\beta$  suggest this will be prevalent at  $z \sim 5$ –8 (Castellano et al. 2017, Harikane et al. 2018, De Barros et al. 2019). JWST will address all these issues with deeper, redder spectra.

## 8. FUTURE PROGRESS WITH JWST

Given its unprecedented ability to study the distant Universe, JWST will undoubtedly revise our understanding of cosmic reionization. To explain how JWST will revolutionize studies of early galaxy formation, we review both the powerful JWST instruments and a subset of the incredible array of Director’s Discretionary-Early Release Science (DD-ERS), Guaranteed Time Observations (GTO), and Cycle 1 Guest Observer (GO) programs planned for the first year of JWST operations.

### 8.1. Overview of JWST Instrumentation

JWST provides four ground-breaking instruments, each with application to cosmic reionization science. We briefly describe the array of instrumentation below, providing information on the field of view, pixel scale, wavelength coverage, observing modes, and typical sensitivities. For reference,  $M^* \approx -21$  galaxies at  $z \sim 8$ –9 have  $f_v \approx 100$  nJy at  $\lambda_{\text{obs}} \approx 1.5$  μm, stellar masses of  $M_* \approx 10^9 M_\odot$  (e.g., Stefanon et al. 2021), and UV line fluxes of  $f \approx 1$ – $5 \times 10^{-18}$  erg s $^{-1}$  cm $^{-2}$  (e.g., Laporte et al. 2021a, Topping et al. 2021).

**8.1.1. MIRI.** The Mid-Infrared Instrument (MIRI; Rieke et al. 2015b, Wright et al. 2015) extends the capabilities of JWST to wavelengths  $\lambda \approx 4.9$ – $28.8$  μm. MIRI includes imaging (Bouchet et al. 2015), coronagraphic (Boccaletti et al. 2015), and spectroscopic (Kendrew et al. 2015, Wells et al. 2015) observing modes. The MIRI detectors are arsenic-doped silicon impurity band

conduction devices (Rieke et al. 2015a). The imaging mode has a  $0.11\text{-arcsec px}^{-1}$  plate scale over a  $74\text{-arcsec} \times 113\text{-arcsec}$  field of view. There are eight broad imaging filters, including F560W ( $\lambda \approx 5.6\text{ }\mu\text{m}$ ), F770W ( $\lambda \approx 7.7\text{ }\mu\text{m}$ ), and F1000W ( $\lambda \approx 10.0\text{ }\mu\text{m}$ ), as well as long-wavelength channel wide filters F1280W ( $\lambda \approx 12.8\text{ }\mu\text{m}$ ), F1500W ( $\lambda \approx 15.0\text{ }\mu\text{m}$ ), F1800W ( $\lambda \approx 18.0\text{ }\mu\text{m}$ ), F2100W ( $\lambda \approx 21.0\text{ }\mu\text{m}$ ), and F2550W ( $\lambda \approx 25.5\text{ }\mu\text{m}$ ). Glasse et al. (2015) presented the predicted sensitivity of MIRI in its various observing modes. For reference,  $\lambda = 7.7\text{ }\mu\text{m}$  (F770W) imaging reaches  $\text{SNR} \approx 10$  point source sensitivities of  $f_v \sim 250\text{ nJy}$  in  $t = 10\text{ ks}$  (see their table 3).

**8.1.2. NIRCam.** The Near Infrared Camera (NIRCam; Rieke et al. 2005) features two HgCdTe detector modules with dichroics to expose short ( $\lambda = 0.6\text{--}2.3\text{ }\mu\text{m}$ ;  $0.031\text{ arcsec px}^{-1}$ ) and long ( $\lambda = 2.4\text{--}5.0\text{ }\mu\text{m}$ ;  $0.063\text{ arcsec px}^{-1}$ ) wavelength channels in parallel. The two detector modules cover  $2.2\text{-arcmin} \times 2.2\text{-arcmin}$  areas ( $9.7\text{ arcmin}^2$  total). NIRCam also enables wide-field slitless spectroscopy at  $\lambda = 2.4\text{--}5.0\text{ }\mu\text{m}$  with  $R \sim 1,600$ , coronagraphy, and photometric and grism time-series observations.

There are 29 NIRCam filters available. For high-redshift photometric studies of faint sources, the short-wavelength channel wide filters F090W ( $\lambda \approx 0.90\text{ }\mu\text{m}$ ), F115W ( $\lambda \approx 1.15\text{ }\mu\text{m}$ ), F150W ( $\lambda \approx 1.50\text{ }\mu\text{m}$ ), and F200W ( $\lambda \approx 2.00\text{ }\mu\text{m}$ ) and long-wavelength channel wide filters F277W ( $\lambda \approx 2.77\text{ }\mu\text{m}$ ), F356W ( $\lambda \approx 3.56\text{ }\mu\text{m}$ ), and F444W ( $\lambda \approx 4.44\text{ }\mu\text{m}$ ) will be frequently used. These filters are complemented by the short-wavelength medium filters F182M ( $\lambda \approx 1.82\text{ }\mu\text{m}$ ) and F210M ( $\lambda \approx 2.10\text{ }\mu\text{m}$ ) and long-wavelength medium filters F335M ( $\lambda \approx 3.35\text{ }\mu\text{m}$ ) and F410M ( $\lambda \approx 4.10\text{ }\mu\text{m}$ ). There are a very large number of additional filters that make NIRCam extremely versatile. NIRCam provides extremely sensitive photometry, reaching  $\text{SNR} \approx 10$  for  $f_v = 10\text{ nJy}$  point sources in  $t \approx 10\text{ ks}$  with F200W.

**8.1.3. NIRISS.** The Near Infrared Imager and Slitless Spectrograph (NIRISS; Doyon et al. 2012) provides wide-field slitless spectroscopy (WFSS;  $\lambda = 0.8\text{--}2.2\text{ }\mu\text{m}$  with  $R \sim 150$  over  $133\text{ arcsec} \times 133\text{ arcsec}$ ), single object slitless spectroscopy ( $\lambda = 0.8\text{--}2.2\text{ }\mu\text{m}$  with  $R \sim 700$ ) in six filters, aperture masking interferometry, and parallel imaging in twelve filters. NIRISS features two grisms that disperse in perpendicular directions, allowing for deblending of spectra from complex source scenes. The NIRISS pixel scale is  $0.065\text{ arcsec px}^{-1}$ . Beyond  $\lambda \approx 1.3\text{ }\mu\text{m}$ , the NIRISS WFSS  $\text{SNR} \approx 10$  line sensitivity is  $F \sim 10^{-17}\text{ erg s}^{-1}\text{ cm}^{-2}$  in  $t = 10\text{ ks}$ . The point source imaging  $\text{SNR} \approx 10$  sensitivity is  $f_v \approx 9.7\text{ nJy}$  in  $t = 10\text{ ks}$  for F200W.

**8.1.4. NIRSpec.** The Near Infrared Spectrograph (NIRSpec; Ferruit et al. 2012) provides prism, medium, and high-resolution spectroscopy at  $\lambda \sim 1\text{--}5\text{ }\mu\text{m}$ . NIRSpec features a microshutter assembly (MSA) consisting of hundreds of thousands of magnetically actuated slitlets. The MSA enables hugely multiplexed ( $\sim$ hundreds of simultaneous targets) multiobject spectroscopy over a  $3.6\text{-arcmin} \times 3.4\text{-arcmin}$  field of view, providing a huge gain in efficiency for rest-frame UV and optical spectroscopy of distant sources. The instrument also features five fixed slits, a  $3\text{-arcsec} \times 3\text{-arcsec}$  integral field unit, and a time-series spectrograph.

There are nine disperser-filter combinations. Four combinations provide  $R \sim 1,000$  spectroscopy over  $\lambda = 0.7\text{--}1.27\text{ }\mu\text{m}$  (G140M/F070LP),  $\lambda = 0.97\text{--}1.84\text{ }\mu\text{m}$  (G140M/F100LP),  $\lambda = 1.66\text{--}3.07\text{ }\mu\text{m}$  (G235M/F170LP), and  $\lambda = 2.87\text{--}5.10\text{ }\mu\text{m}$  (G395M/F290LP) wavelength ranges. The four high-resolution disperser-filter combinations enable  $\lambda = 0.81\text{--}1.27\text{ }\mu\text{m}$  (G140H/F070LP),  $\lambda = 0.97\text{--}1.82\text{ }\mu\text{m}$  (G140H/F100LP),  $\lambda = 1.66\text{--}3.05\text{ }\mu\text{m}$  (G235H/F170LP), and  $\lambda = 2.87\text{--}5.14\text{ }\mu\text{m}$  (G395H/F290LP) spectroscopy at  $R \sim 2,700$ . The PRISM/CLEAR combination provides  $R \sim 100$  spectroscopy over the wide wavelength range  $\lambda = 0.60\text{--}5.30\text{ }\mu\text{m}$ .

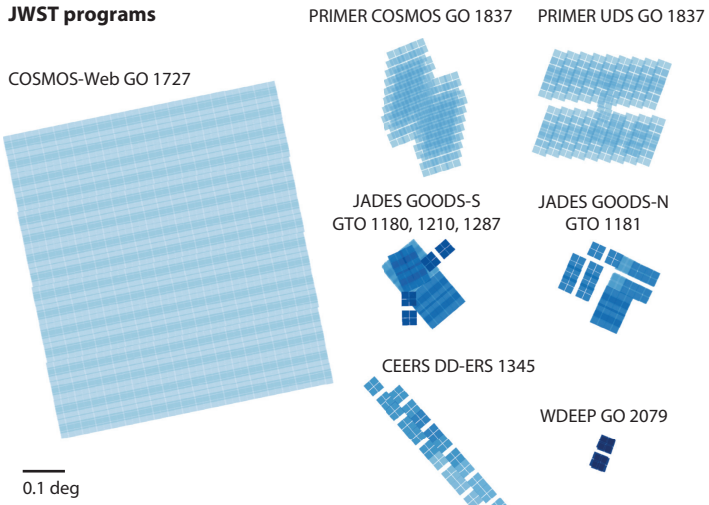


**Figure 6**

Approximate NIRCam prime and parallel exposure maps for a subset of extragalactic programs planned during Cycle 1 with JWST relevant for studies of cosmic reionization. These programs include COSMOS-Web (GO 1727), JADES GOODS-N (GTO 1181), and GOODS-S (GTO 1180, 1210, 1287 shown; GTO 1286 parallels omitted) fields, PRIMER COSMOS and Ultra Deep Survey fields (GO 1837), CEERS (DD-ERS 1345) in the EGS field, and WDEEP (GO 2079) on UDF Parallel 2. The maps are extracted from the public APT data available for each program and represent the relative exposure time and coverage of their F115W or F200W imaging.

## 8.2. JWST Programs

During Cycle 1, JWST will execute a wide range of observing programs focused on extragalactic science. Here, we discuss an incomplete subset of the DD-ERS, GTO, and GO programs relevant for studies of the distant Universe. **Figure 6** shows approximate NIRCam F115W or F200W exposure maps for a subset of these DD-ERS, GTO, and GO programs computed from their public Astronomer's Proposal Tool (APT) files. Each program in **Figure 6** is reviewed below. In each case, the programs are presented in order of their Program ID and information about the observations summarized from the APT files and Phase2 Public abstracts. The relative areas of the observed fields should be accurate, and the color scale indicates the relative exposure times in each field.

**8.2.1. Director's discretionary early release science programs.** The substantial investment of public DD-ERS programs will provide an important community resource of public JWST data that exercise the instrumentation. For cosmic reionization science, the DD-ERS programs that expose early deep imaging in fields with supporting ancillary data, that provide demonstrations of the JWST instrument performance on fields with key extragalactic targets, or that showcase the new IR spectroscopy capabilities of JWST on objects of interest will prove most useful. Here, we describe two JWST DD-ERS programs particularly relevant for cosmic reionization research.

Through the Looking GLASS (DD-ERS 1324, 35.1 h; Treu et al. 2017) will expose NIRISS WFSS, NIRSpec MSA, and NIRCam on the Frontier Fields gravitational lensing cluster Abell 2744. The NIRISS and NIRSpec prime observations cover a single pointing, with the NIRISS data probing  $\lambda = 1\text{--}2.2 \mu\text{m}$  with the  $R = 150$  grism ( $m_{AB} \approx 25.5\text{--}26.3$  per pixel) and with direct images ( $m_{AB} \sim 27.5\text{--}27.8$ ). Their NIRSpec observations use the high-resolution gratings at

$\lambda \approx 0.97\text{--}5.14 \mu\text{m}$  at  $t_{\text{exp}} \approx 17.7$  ks per band. The NIRCam parallel observations cover two nearby fields in F090W, F115W, F150W, F200W, F277W, F356W, and F444W with exposure times weighted to reach  $m_{\text{AB}} \approx 29\text{--}29.4$  in each filter.

The Cosmic Evolution Early Release Science (CEERS) program (DD-ERS 1345, 65.7 h; Finkelstein et al. 2017) will observe  $\approx 100$  arcmin $^2$  in the Extended Groth Strip with NIRCam and MIRI imaging and with NIRSpec MSA and NIRCam WFSS spectroscopy. CEERS will conduct parallel observations, exposing in NIRCam with parallel imaging while prime observing with NIRSpec or MIRI. The CEERS NIRCam coverage includes F115W, F150W, F200W, F277W, F356W, F410M, and F444W, with  $t_{\text{exp}} \approx 2.8$  ks in each ( $t_{\text{exp}} \approx 5.7$  ks in F150W). The NIRCam WFSS uses F356W. MIRI exposures include F1000W, F1280W, F1500W, F1800W, and F2100W. NIRSpec coverage in CEERS features the medium-resolution ( $R \sim 1,000$ ) grating with wavelength coverage  $\lambda \approx 0.97\text{--}5.14 \mu\text{m}$  ( $t_{\text{exp}} \approx 2.9$  ks), and  $R \sim 100$  prism observations with  $m_{\text{AB}} \approx 26.5$  continuum sensitivity. An approximate exposure map of the CEERS F200W imaging is provided in **Figure 6**.

Additional relevant DD-ERS programs include TEMPLATES: Targeting Extremely Magnified Panchromatic Lensed Arcs and Their Extended Star formation (DD-ERS 1355; Rigby et al. 2017).

**8.2.2. Guaranteed time observations.** Each of the JWST instrument teams and interdisciplinary scientists received GTO. The GTO program covers an extremely wide range of science, well beyond the cosmic reionization focus of this review, including the ISM, exoplanet research, and stellar population investigations. The GTO programs for extragalactic science feature incredibly powerful combinations of filter arrays, spectroscopic modes, depths, and parallel observations. Given the sensitivity of JWST to distant galaxies, nearly all of the extragalactic GTO surveys are relevant for studying galaxies during cosmic reionization.

The NIRCam–NIRSpec joint GTO program called JWST Advanced Deep Extragalactic Survey (JADES) will survey GOODS-North and GOODS-South with a wide range of NIRCam, MIRI, and NIRSpec observations. The design of the GOODS-S survey involves a series of NIRSpec prime–NIRCam parallel observations, followed by NIRCam prime–MIRI parallel imaging, and concluding with another set NIRSpec prime–NIRCam parallel exposures. There are two characteristic NIRCam exposure depths for JADES wide-band imaging, including deep imaging at  $m_{\text{AB}} \approx 29.8\text{--}30.35$  over  $\sim 46$  arcmin $^2$  and medium imaging at  $m_{\text{AB}} \approx 29.0\text{--}29.5$  over  $\sim 290$  arcmin $^2$ . NIRCam images in JADES all include short-wavelength filters F090W, F115W, F150W, and F200W and long-wavelength filters F277W, F356W, F410M, and F444W. Additional medium band images in F335M are acquired over subsets of the field to  $\approx 0.8$  AB lower sensitivity, and we note that the F410M and F444W images are shallower than the other broadbands by  $\sim 0.2\text{--}0.5$  AB (but can be combined to match the deep depths). NIRSpec observations are acquired with the prism, medium-resolution spectroscopy with F070LP, F170LP, and F290LP and high-resolution spectroscopy with F290LP. **Figure 6** shows approximate F200W exposure maps for the JADES GOODS-N and GOODS-S regions, where the relative subfield locations will depend on the actual position angle of the observations.

The JADES GOODS-S observations are acquired through several GTO Program IDs. Initial NIRSpec observations (GTO 1210, 74.2 h; Ferruit 2017a) are acquired in a single region targeting known objects near the HUDF, using prism, medium, and high-resolution spectroscopy. In parallel, deep NIRCam images are acquired at a single location. A compact NIRCam mosaic of deep and medium exposures is then created (GTO 1180, 355.7 h; Eisenstein et al. 2017b). A set of medium NIRSpec exposures near the HUDF are acquired, along with medium NIRCam parallels arranged into a mosaic. A set of deep and medium NIRCam prime images then completes the

contiguous mosaic while exposing in MIRI F777W and F1280W. Two later sets of additional NIRSpec pointings then visit the NIRCam mosaic, exposing the medium (GTO 1286, 149.3 h; Ferruit et al. 2017a) and deep (GTO 1287, 74.2 h; Ferruit & Rieke 2017b) regions while imaging with NIRCam in parallel. Note that **Figure 6** does not show the parallel NIRCam fields from GTO 1286, which can be arranged into a rough mosaic in GOODS-S depending on when the field is observed.

In JADES GOODS-N (GTO 1181, 152.8 h; Eisenstein et al. 2017a), a region will be exposed with NIRCam prime with MIRI parallel (F770W and F1280W) to medium depth. Initial NIRSpec pointings targeted from HST sources in GOODS-N will be acquired with NIRCam in parallel to continue the compact medium depth mosaic with the same filters. The NIRSpec pointings will use the prism and the medium-resolution disperser with F070LP, F170LP, and F290LP. Sources from the initial NIRCam GOODS-N area will then be revisited with NIRSpec pointings that additionally include high-resolution spectroscopy in F290LP. NIRCam parallels will be taken in a nearby region of CANDELS GOODS-N to medium depth. The NIRCam images in GOODS-N cover the Hubble Deep Field-N region.

As part of the GTO team efforts, the JADES collaboration has been performing detailed simulations of their survey data. Using the JAGUAR (JAdes ExtraGalactic Ultra-deep Artificial Realization) synthetic galaxy catalog (Williams et al. 2018) and the Guitarra image simulation code (Willmer et al. 2020), the NIRCam GTO JADES team has produced an end-to-end model of the individual ramps, distortion, mosaicing, pixel-level error propagation, detection, and photometry for JADES. The NIRSpec GTO JADES team then performs spectroscopic source selection and simulated spectroscopy. **Figure 7** shows a false-color visualization of a simulated F090W-F115W-F444W multiband image (JADES Collab., private communication, adapted from Williams et al.



**Figure 7**

Zoomed region of a simulation of the JADES Deep imaging region in GOOD-S. Shown is a F090W-F115W-F444W false-color image created from synthetic data produced with the Guitarra (Willmer et al. 2020) image simulator and processed with the JADES mosaicing and analysis pipeline. JADES Deep NIRCam imaging will reach  $f_v \approx 29.4\text{--}30.35$  AB magnitude limits ( $5\sigma$ ) for the  $\lambda \approx 0.90\text{--}4.4\mu\text{m}$  broadband filters. Figure adapted from Williams et al. (2018) with permission.

2018). The depth achievable by JWST is illustrated by the richness of the structures in this simulated image, which corresponds to a  $5 - \sigma$  sensitivity of  $m_{AB} = 30.35$  in F115W.

There are two MIRI programs targeting the HUDF. Program GTO 1207 (89.7 h; Rieke et al. 2017, 2019) will observe the HUDF region with a  $\approx 30\text{-arcmin}^2$  mosaic using all the MIRI imaging bands, and follow up with  $R = 1,000$  NIRSpec spectroscopy at  $\lambda = 0.97\text{--}5.14\text{ }\mu\text{m}$ . Program GTO 1283 (60.9 h; Norgaard-Nielsen & Perez-Gonzalez 2017) will image the HUDF with a single pointing in F560W for 60 h, reaching  $m_{AB} \sim 28.3$  ( $SNR = 4$ ). Parallel observations will be acquired with NIRCam (F115W, F277W, F356W) for 40 h and NIRISS (F115W, F150W, and F200W at  $R \sim 150$ ) for 20 h in nearby regions of GOODS-S.

Additional programs related to cosmic reionization include the Interdisciplinary Scientist GTO Programs (GTO 1176, Windhorst et al. 2017; GTO 1243, Lilly et al. 2017), CANUCS: the Canadian NIRISS Unbiased Cluster Survey (NIRISS, GTO 1208; Willott et al. 2017a), the Cosmic Re-ionization, Metal Enrichment, and Host Galaxies from Quasar Spectroscopy (NIRSpec, GTO 1222; Willott et al. 2017b), and the NIRSpec WIDE survey (GTO 1211–1215; Ferruit 2017b,c,d,e).

**8.2.3. Guest observer programs.** A series of JWST GO programs will pursue extremely ambitious cosmic reionization science. There are roughly three dozen GO extragalactic programs that explore distant galaxies near reionization. Below, we discuss five and note several others.

COSMOS-Web (GO 1727, 207.8 h; Kartaltepe et al. 2021) is the largest targeted extragalactic GO program, both in time and area, covering approximately  $\sim 0.6\text{ deg}^2$  with NIRCam and  $\sim 0.2\text{ deg}^2$  with MIRI. The NIRCam images expose F115W, F150W, F277W, and F444W to  $m_{AB} \approx 27.4\text{--}28.0$ , whereas MIRI exposes in parallel F770W to  $m_{AB} \approx 24.3\text{--}24.5$ . **Figure 6** shows the F115W exposure map for COSMOS-Web. The extreme area will enable COSMOS-Web to discover rare, bright objects during cosmic reionization, whereas the contiguous mosaic will allow for detailed clustering of high-redshift galaxies.

The Public Release IMaging for Extragalactic Research (GO 1837, 188.1 h; Dunlop et al. 2021) survey will observe the HST CANDELS regions in COSMOS and Ultra Deep Survey (UDS). The designs of the two mosaics are carefully orchestrated to provide substantial overlap between the MIRI prime imaging and the NIRCam parallel imaging. The NIRCam (MIRI) mosaics are  $144\text{ arcmin}^2$  ( $112\text{ arcmin}^2$ ) in COSMOS and  $234\text{ arcmin}^2$  ( $125\text{ arcmin}^2$ ) in UDS, and each field has a NIRCam–MIRI overlap area of more than  $100\text{ arcmin}^2$ . The PRIMER NIRCam images use F090W, F115W, F150W, and F200W, F277W, F356W, F410M, and F444W, and will reach  $m_{AB} \approx 28.5\text{--}29.5$  (F200W). The MIRI images use F770W and F1800W to reach  $m_{AB} \approx 25.6$  in F770W. **Figure 6** shows approximate exposure maps for the PRIMER F200W imaging in COSMOS and the UDS, constructed from the public APT files.

The Webb Deep Extragalactic Exploratory Public (WDEEP) Survey (GO 2079, 121.7 h; Finkelstein et al. 2021) uses extremely sensitive observations with NIRISS in the HUDF and NIRCam on HUDF Parallel 2. The WDEEP NIRISS observations will reach line sensitivities of  $f_v \approx 10^{-18}\text{ erg s}^{-1}\text{ cm}^{-2}$  in F115W, F150W, and F200W grism observations, covering the extremely deep HST/ACS (Advanced Camera for Surveys) imaging conducted in the HUDF. WDEEP can leverage the ultradeep F814W HST imaging in HUDF Parallel 2 from the UDF12 (2012 Hubble Ultra Deep Field) project (Ellis et al. 2013) as a veto for its deep NIRCam F115W, F150W, F200W, F356W, and F444W images in conducting high-redshift galaxy searches to  $m_{AB} \sim 30.6\text{--}30.9$ . The NIRCam imaging area is slightly larger than a single pointing, and an approximate exposure map for WDEEP is shown in **Figure 6**.

The First Reionization Epoch Spectroscopic COmplete Survey (FRESCO; GO 1895, 53.1h; Oesch et al. 2021) will conduct F444W NIRCam grism observations in two mosaics, each

covering a 60-arcmin<sup>2</sup> region of GOODS-N or GOODS-S. FRESCO will reach a line sensitivity of roughly  $f_v \approx 3 \times 10^{-18}$  erg s<sup>-1</sup> cm<sup>-2</sup>, allowing for the identification of more than 300 galaxies at  $z > 7$ . By using the grism, FRESCO can attempt to capture the rest-frame optical emission of high-redshift galaxies with an effectively flux-limited selection, which will provide an interesting view into the star formation and internal ionizing radiation fields of distant sources.

The Ultra-deep NIRCam and NIRSpec Observations Before the Epoch of Reionization (UNCOVER; GO 2561, 68.2 h; Labbe et al. 2021) will image the gravitational lensing cluster Abell 2744 in NIRCam F115W, F150W, F200W, F277W, F356W, F410M, and F444W to  $m_{AB} \approx 29.8$ , followed by extremely deep  $t_{exp} \approx 19$  h NIRSpec prism spectroscopy. The program will obtain deep parallel NIRISS and NIRCam imaging in a nearby field. UNCOVER will establish one of the intrinsically deepest observations with JWST, with the ability to probe further down the high-redshift luminosity function than larger area surveys.

JWST will conduct many other notable GO programs relevant for cosmic reionization. We briefly mention an incomplete list here. Two pure parallel programs, PASSAGE (Parallel Application of Slitless Spectroscopy to Analyze Galaxy Evolution (GO 1571, 591 h; Malkan et al. 2021) with NIRISS and PANORAMIC (a Pure Parallel Wide Area Legacy Imaging Survey at 1-5 Micron) (GO 2514, 150 h; Williams et al. 2021b) with NIRCam will observe a large area and potentially find many bright, high-redshift galaxies. The spectroscopic programs AURORA (GO 1914, 63.8 h; Shapley et al. 2021) and CECILIA (Chemical Evolution Constrained using Ionized Lines in Interstellar Aurorae) (GO 2593, 39.2 h; Strom et al. 2021) will provide direct-method calibrations of high-redshift galaxy metallicities, which will inform models for the ionizing photon production efficiency. The UDF Medium Band survey (GO 1963, 20.4 h; Williams et al. 2021a) will provide NIRCam imaging in the HUDF with F182M, F210M, F430M, F460M, and F480M, along with NIRISS F430M and F480M imaging in parallel. At least two programs will perform spectroscopy on LyC-emitting galaxies, including NIRSpec/IFU (Integral Field Unit) observations (GO 1827, 24.1 h; Kakiichi et al. 2021) and NIRSpec medium-resolution spectroscopy (GO 1869, 73.5 h; Schaefer et al. 2021), both observing  $z \sim 3$  strong-line emitters.

## 9. SUMMARY

Over the last 5–10 years, our knowledge of galaxy formation during cosmic reionization has advanced dramatically. The discovery of photometric candidates at  $z \sim 6$ –10 with HST and other facilities has revealed a substantial population of galaxies forming just a few hundred million years after the Big Bang. The spectroscopic confirmation of very distant galaxies out to  $z \sim 8$ –10.5 has now solidified the reality of these early objects. With the coming of JWST, which will find more and fainter galaxies during reionization and measure their rest-frame optical spectra, we will begin to understand the physics behind the role galaxies play in cosmic reionization. Instead of wondering whether galaxies dominated cosmic reionization, research questions will focus on the physical mechanisms by which galaxies produce and release LyC radiation and the properties of the galaxy population. JWST will help us answer how galaxies were able to rewrite cosmic history by reionizing the Universe.

### SUMMARY POINTS

1. Deep, near-IR surveys have now established that galaxies primarily reionized the Universe, and radiation from accretion onto supermassive black holes in AGNs plays a less dominant role.

2. The UV luminosity density declines from  $z \sim 6$ –10, but the continued decline beyond  $z \sim 10$  is still unconfirmed.
3. Our understanding of the ability for stellar populations to produce efficiently ionizing photons has substantially improved, guided by both population synthesis modeling and observational evidence for strong nebular emission in distant galaxies.
4. The escape of Lyman continuum (LyC) photons from galaxies during cosmic reionization is complex and remains a challenge for understanding the detailed physics of the reionization process.
5. The discovery of very bright, distant galaxies during the epoch of reionization may rebalance conclusions about the relative importance of bright versus faint galaxies in cosmic reionization.
6. Redshift confirmation of distant galaxies at redshifts  $z \sim 8$ –10 has established the reality of star-forming systems less than 500 Myr after the Big Bang.
7. Stellar mass function constraints at high redshift are improving, and the presence of evolved stars in early galaxies provide circumstantial evidence for extended star formation to  $z \sim 15$  that the *James Webb Space Telescope* (JWST) could potentially verify.

## FUTURE ISSUES

1. JWST will provide a revolutionary facility for studying cosmic reionization and will execute many exciting programs in its first year of operations.
2. The complexity of the JWST data, including in the wide range of sensitive photometric filters, the power of wide-field slitless spectroscopy, and the new advance of highly multiplexed IR spectroscopy in space, will present a rewarding challenge for the astronomical community.
3. JWST can discover and potentially confirm galaxies out to extraordinarily high redshifts, but it remains unclear, given the decline of the high-redshift luminosity density, how many galaxies beyond  $z \sim 10$  will be newly revealed.
4. The ability to measure rest-frame optical spectra, estimate ionizing photon production through nebular emission, and constrain evolved stellar populations in galaxies at redshifts  $z > 8$  will place an increased emphasis on the detailed modeling of early galaxy evolution.
5. Questions about the evolution of the LyC escape fraction, how it depends on galaxy properties including the efficiency of ionizing photon production, will remain an area of active research.
6. Understanding and interpreting the detailed spectra of distant galaxies will provide a rich area for exploring cosmic reionization with JWST, including studies of the excitation of near-UV metal lines, the propagation of Ly $\alpha$ , the connection between interstellar absorption and LyC escape, direct calibration of metallicity indicators, and the connection between metallicity and ionizing photon production.

## DISCLOSURE STATEMENT

The author is not aware of any affiliations, memberships, funding, or financial holdings that might be perceived as affecting the objectivity of this review.

## ACKNOWLEDGMENTS

B.E.R. thanks Sandy Faber for carefully reading the manuscript and providing detailed comments that improved this review. Thanks to Pascal Oesch and Christina Williams for permission to use or adapt their figures, and Rychard Bouwens for providing the data in **Figure 3**. Thanks also to the JADES collaboration for providing **Figure 7**, with special thanks to Sandro Tacchella, Christopher Willmer, and Marcia Rieke. Also, thanks to Anton Koekemoer for providing the updated ATP file for COSMOS-Web. B.E.R. acknowledges support from NASA contract NNG16PJ25C and grant number 80NSSC18K0563.

## LITERATURE CITED

- Alavi A, Colbert J, Teplitz HI, et al. 2020. *Ap. J.* 904:59
- Alexandroff RM, Heckman TM, Borthakur S, Overzier R, Leitherer C. 2015. *Ap. J.* 810(2):104
- Atek H, Richard J, Jauzac M, et al. 2015. *Ap. J.* 814:69
- Bañados E, Venemans BP, Mazzucchelli C, et al. 2018. *Nature* 553(7689):473–76
- Bagley MB, Scarlata C, Henry A, et al. 2017. *Ap. J.* 837:11
- Bakx TJLC, Tamura Y, Hashimoto T, et al. 2020. *MNRAS* 493(3):4294–307
- Barrow KSS, Robertson BE, Ellis RS, et al. 2020. *Ap. J. Lett.* 902(2):L39
- Bassett R, Ryan-Weber EV, Cooke J, et al. 2021. *MNRAS* 502:108–26
- Behroozi P, Conroy C, Wechsler RH, et al. 2020. *MNRAS* 499(4):5702–18
- Bhatawdekar R, Conselice CJ, Margalef-Bentabol B, Duncan K. 2019. *MNRAS* 486(3):3805–30
- Boccaletti A, Lagage PO, Baudoz P, et al. 2015. *Proc. Astron. Soc. Pac.* 127(953):633
- Boera E, Becker GD, Bolton JS, Nasir F. 2019. *Ap. J.* 872:101
- Bose S, Deason AJ, Frenk CS. 2018. *Ap. J.* 863(2):123
- Bosman SEI, Kakiichi K, Meyer RA, et al. 2020. *Ap. J.* 896:49
- Bouchet P, García-Marín M, Lagage PO, et al. 2015. *Proc. Astron. Soc. Pac.* 127(953):612
- Bouwens RJ, Oesch PA, Illingworth GD, Ellis RS, Stefanon M. 2017. *Ap. J.* 843(2):129
- Bouwens RJ, Oesch PA, Stefanon M, et al. 2021a. *Astron. J.* 162(2):47
- Bouwens RJ, Smit R, Labbé I, et al. 2016. *Ap. J.* 831(2):176
- Bouwens RJ, Smit R, Schouws S, et al. 2021b. *Ap. J.* 931(2):160
- Bowler RAA, Dunlop JS, McLure RJ, McLeod DJ. 2017. *MNRAS* 466(3):3612–35
- Bowler RAA, Dunlop JS, McLure RJ, et al. 2015. *MNRAS* 452(2):1817–40
- Bowler RAA, Jarvis MJ, Dunlop JS, et al. 2020. *MNRAS* 493(2):2059–84
- Bradač M. 2020. *Nat. Astron.* 4:478–85
- Bradač M, Garcia-Appadoo D, Huang KH, et al. 2017. *Ap. J. Lett.* 836:L2
- Bradač M, Ryan R, Casertano S, et al. 2014. *Ap. J.* 785(2):108
- Bradley LD, Trenti M, Oesch PA, et al. 2012. *Ap. J.* 760(2):108
- Bridge JS, Holwerda BW, Stefanon M, et al. 2019. *Ap. J.* 882:42
- Calvi V, Trenti M, Stiavelli M, et al. 2016. *Ap. J.* 817(2):120
- Carniani S, Maiolino R, Pallottini A, et al. 2017. *Astron. Astrophys.* 605:A42
- Casey CM, Narayanan D, Cooray A. 2014. *Phys. Rep.* 541(2):45–161
- Castellano M, Pentericci L, Fontana A, et al. 2017. *Ap. J.* 839(2):73
- Chabrier G. 2003. *Proc. Astron. Soc. Pac.* 115(809):763–95
- Chisholm J, Gazagnes S, Schaerer D, et al. 2018. *Astron. Astrophys.* 616:A30
- Chisholm J, Orlitová I, Schaerer D, et al. 2017. *Astron. Astrophys.* 605:A67
- Choi Y, Dalcanton JJ, Williams BF, et al. 2020. *Ap. J.* 902:54

- Coe D, Salmon B, Bradač M, et al. 2019. *Ap. J.* 884:85
- Conselice CJ, Wilkinson A, Duncan K, Mortlock A. 2016. *Ap. J.* 830(2):83
- D'Aloisio A, Upton Sanderbeck PR, McQuinn M, Trac H, Shapiro PR. 2017. *MNRAS* 468(4):4691–701
- Davidzon I, Ilbert O, Laigle C, et al. 2017. *Astron. Astrophys.* 605:A70
- Davies FB, Hennawi JF, Bañados E, et al. 2018. *Ap. J.* 864(2):142
- Dayal P, Volonteri M, Choudhury TR, et al. 2020. *MNRAS* 495(3):3065–78
- De Barros S, Oesch PA, Labbé I, et al. 2019. *MNRAS* 489(2):2355–66
- de Barros S, Vanzella E, Amorín R, et al. 2016. *Astron. Astrophys.* 585:A51
- Doyon R, Hutchings JB, Beaulieu M, et al. 2012. *Proc. SPIE Conf. Ser.* 8442:84422R
- Duncan K, Conselice CJ. 2015. *MNRAS* 451(2):2030–49
- Duncan K, Conselice CJ, Mortlock A, et al. 2014. *MNRAS* 444(3):2960–84
- Dunlop JS, Abraham RG, Ashby MLN, et al. 2021. *PRIMER: Public Release IMaging for Extragalactic Research.* JWST Proposal. Cycle 1
- Dunlop JS, McLure RJ, Biggs AD, et al. 2017. *MNRAS* 466:861–83
- Eisenstein DJ, Ferruit P, Rieke MJ. 2017a. *NIRCam-NIRSpec galaxy assembly survey - GOODS-N.* JWST Proposal. Cycle 1
- Eisenstein DJ, Ferruit P, Rieke MJ, Willmer CNA, Willott CJ. 2017b. *NIRCam-NIRSpec galaxy assembly survey - GOODS-S - part #1a.* JWST Proposal. Cycle 1
- Eldridge JJ, Stanway ER, Xiao L, et al. 2017. *Proc. Astron. Soc. Aust.* 34:e058
- Ellis RS, McLure RJ, Dunlop JS, et al. 2013. *Ap. J. Lett.* 763:L7
- Emami N, Siana B, Alavi A, et al. 2020. *Ap. J.* 895(2):116
- Endsley R, Stark DP, Charlot S, et al. 2021a. *MNRAS* 502(4):6044–63
- Endsley R, Stark DP, Chevallard J, Charlot S. 2021b. *MNRAS* 500(4):5229–48
- Fan X, Carilli CL, Keating B. 2006. *Annu. Rev. Astron. Astrophys.* 44:415–62
- Feltre A, Charlot S, Gutkin J. 2016. *MNRAS* 456(3):3354–74
- Ferruit P. 2017a. *NIRCam-NIRSpec galaxy assembly survey - GOODS-S - part #1b.* JWST Proposal. Cycle 1
- Ferruit P. 2017b. *NIRSpec WIDE MOS Survey - AEGIS.* JWST Proposal. Cycle 1
- Ferruit P. 2017c. *NIRSpec WIDE MOS Survey - COSMOS.* JWST Proposal. Cycle 1
- Ferruit P. 2017d. *NIRSpec WIDE MOS Survey - GOODS-N.* JWST Proposal. Cycle 1
- Ferruit P. 2017e. *NIRSpec WIDE MOS Survey - UDS.* JWST Proposal. Cycle 1
- Ferruit P, Bagnasco G, Barho R, et al. 2012. *Proc. SPIE Conf. Ser.* 8442:84422O
- Ferruit P, Eisenstein DJ, Rieke MJ, Willott CJ. 2017a. *NIRCam-NIRSpec galaxy assembly survey - GOODS-S - part #2.* JWST Proposal. Cycle 1
- Ferruit P, Rieke MJ. 2017b. *NIRCam-NIRSpec galaxy assembly survey - GOODS-S - part #3.* JWST Proposal. Cycle 1
- Finkelstein SL, Bagley M, Song M, et al. 2022. *Ap. J.* 928:52
- Finkelstein SL, D'Aloisio A, Paardekooper JP, et al. 2019. *Ap. J.* 879:36
- Finkelstein SL, Dickinson M, Ferguson HC, et al. 2017. *The Cosmic Evolution Early Release Science (CEERS) Survey.* JWST Proposal ID 1345. Cycle 0 Early Release Science
- Finkelstein SL, Papovich C, Dickinson M, et al. 2013. *Nature* 502(7472):524–27
- Finkelstein SL, Papovich C, Pirzkal N, et al. 2021. *The Webb Deep Extragalactic Exploratory Public (WDEEP) Survey: Feedback in Low-Mass Galaxies from Cosmic Dawn to Dusk.* JWST Proposal. Cycle 1
- Finlator K, Oh SP, Özel F, Davé R. 2012. *MNRAS* 427(3):2464–79
- Fletcher TJ, Tang M, Robertson BE, et al. 2019. *Ap. J.* 878(2):87
- Franco M, Elbaz D, Béthermin M, et al. 2018. *Astron. Astrophys.* 620:A152
- Fuller S, Lemaux BC, Bradač M, et al. 2020. *Ap. J.* 896(2):156
- Furtak LJ, Atek H, Lehnert MD, Chevallard J, Charlot S. 2021. *MNRAS* 501(2):1568–90
- Gazagnes S, Chisholm J, Schaeerer D, Verhamme A, Izotov Y. 2020. *Astron. Astrophys.* 639:A85
- Giallongo E, Grazian A, Fiore F, et al. 2015. *Astron. Astrophys.* 578:A83
- Glasse A, Rieke GH, Bauwens E, et al. 2015. *Proc. Astron. Soc. Pac.* 127(953):686
- Gnedin NY. 2014. *Ap. J.* 793:29
- Gnedin NY. 2016. *Ap. J. Lett.* 825(2):L17

- Gnedin NY, Kaurov AA. 2014. *Ap. J.* 793:30
- Gorce A, Douspis M, Aghanim N, Langer M. 2018. *Astron. Astrophys.* 616:A113
- Grazian A, Fontana A, Santini P, et al. 2015. *Astron. Astrophys.* 575:A96
- Grazian A, Giallongo E, Boutsia K, et al. 2018. *Astron. Astrophys.* 613:A44
- Guaita L, Pentericci L, Grazian A, et al. 2016. *Astron. Astrophys.* 587:A133
- Harikane Y, Laporte N, Ellis RS, Matsuoka Y. 2020. *Ap. J.* 902(2):117
- Harikane Y, Ono Y, Ouchi M, et al. 2022. *Ap. J. Suppl. Ser.* 259:20
- Harikane Y, Ouchi M, Shibuya T, et al. 2018. *Ap. J.* 859(2):84
- Hashimoto T, Inoue AK, Mawatari K, et al. 2019. *Proc. Astron. Soc. Jpn.* 71(4):71
- Hashimoto T, Laporte N, Mawatari K, et al. 2018. *Nature* 557(7705):392–95
- Hassan S, Davé R, Mitra S, Finlator K, Ciardi B, Santos MG. 2018. *MNRAS* 473:227–40
- Hernán-Caballero A, Pérez-González PG, Diego JM, et al. 2017. *Ap. J.* 849(2):82
- Hoag A, Bradač M, Huang K, et al. 2019. *Ap. J.* 878:12
- Hoag A, Bradač M, Trenti M, et al. 2017. *Nat. Astron.* 1:0091
- Hodge JA, Karim A, Smail I, et al. 2013. *Ap. J.* 768:91
- Hutchison TA, Papovich C, Finkelstein SL, et al. 2019. *Ap. J.* 879(2):70
- Inoue AK, Shimizu I, Iwata I, Tanaka M. 2014. *MNRAS* 442(2):1805–20
- Inoue AK, Tamura Y, Matsuo H, et al. 2016. *Science* 352(6293):1559–62
- Ishigaki M, Kawamata R, Ouchi M, et al. 2018. *Ap. J.* 854:73
- Izotov YI, Orlitová I, Schaerer D, et al. 2016a. *Nature* 529(7585):178–80
- Izotov YI, Schaerer D, Thuan TX, et al. 2016b. *MNRAS* 461(4):3683–701
- Izotov YI, Schaerer D, Worseck G, et al. 2020. *MNRAS* 491:468–82
- Izotov YI, Thuan TX, Guseva NG. 2017. *MNRAS* 471:548–61
- Izotov YI, Worseck G, Schaerer D, et al. 2018. *MNRAS* 478(4):4851–65
- Izotov YI, Worseck G, Schaerer D, et al. 2021. *MNRAS* 503(2):1734–52
- Izumi T, Matsuoka Y, Fujimoto S, et al. 2021. *Ap. J.* 914:36
- Japelj J, Vanzella E, Fontanot F, et al. 2017. *MNRAS* 468:389–403
- Jaskot AE, Ravindranath S. 2016. *Ap. J.* 833(2):136
- Jiang L, Kashikawa N, Wang S, et al. 2021. *Nat. Astron.* 5:256–61
- Jones LH, Barger AJ, Cowie LL. 2021. *Ap. J.* 908(2):222
- Jones T, Sanders R, Roberts-Borsani G, et al. 2020. *Ap. J.* 903(2):150
- Jung I, Finkelstein SL, Dickinson M, et al. 2019. *Ap. J.* 877(2):146
- Jung I, Finkelstein SL, Dickinson M, et al. 2020. *Ap. J.* 904(2):144
- Kakiichi K, Ellis RS, Hennawi J, et al. 2021. *NIRSpec Integral Field Spectroscopy of LyC-Leaking Galaxies*. JWST Proposal. Cycle 1
- Kakiichi K, Ellis RS, Laporte N, et al. 2018. *MNRAS* 479:43–63
- Kakiichi K, Gronke M. 2021. *Ap. J.* 908:30
- Kartaltepe J, Casey CM, Bagley M, et al. 2021. *COSMOS-Webb: The Webb Cosmic Origins Survey*. JWST Proposal. Cycle 1
- Katz H, Kimm T, Haehnelt M, Sijacki D, Rosdahl J, Blaizot J. 2018. *MNRAS* 478(4):4986–5005
- Kawamata R, Ishigaki M, Shimasaku K, et al. 2018. *Ap. J.* 855:4
- Kendrew S, Scheithauer S, Bouchet P, et al. 2015. *Proc. Astron. Soc. Pac.* 127(953):623
- Khaire V, Srianand R, Choudhury TR, Gaikwad P. 2016. *MNRAS* 457(4):4051–62
- Kikuchihara S, Ouchi M, Ono Y, et al. 2020. *Ap. J.* 893:60
- Kulkarni G, Worseck G, Hennawi JF. 2019. *MNRAS* 488:1035–65
- Labbe I, Bezanson R, Atek H, et al. 2021. *UNCOVER: Ultra-deep NIRCam and NIRSpec Observations Before the Epoch of Reionization*. JWST Proposal. Cycle 1
- Labbé I, Oesch PA, Illingworth GD, et al. 2015. *Ap. J. Suppl. Ser.* 221(2):23
- Lagache G, Cousin M, Chatzikos M. 2018. *Astron. Astrophys.* 609:A130
- Lam D, Bouwens RJ, Labbé I, et al. 2019. *Astron. Astrophys.* 627:A164
- Lapi A, Mancuso C, Celotti A, Danese L. 2017. *Ap. J.* 835:37
- Laporte N, Katz H, Ellis RS, et al. 2019. *MNRAS* 487:L81–85

- Laporte N, Meyer RA, Ellis RS, et al. 2021a. *MNRAS* 505(3):3336–46
- Laporte N, Nakajima K, Ellis RS, et al. 2017. *Ap. J.* 851:40
- Laporte N, Zitrin A, Ellis RS, et al. 2021b. *MNRAS* 505(4):4838–46
- Larson RL, Finkelstein SL, Pirzkal N, et al. 2018. *Ap. J.* 858(2):94
- Lewis JSW, Ocvirk P, Aubert D, et al. 2020. *MNRAS* 496(4):4342–57
- Lilly SJ, Bordoloi R, Kashino D, Simcoe RA. 2017. *Exploring the End of Cosmic Reionization*. JWST Proposal. Cycle 1
- Liu C, Mutch SJ, Angel PW, et al. 2016. *MNRAS* 462:235–49
- Livermore RC, Finkelstein SL, Lotz JM. 2017. *Ap. J.* 835(2):113
- Livermore RC, Trenti M, Bradley LD, et al. 2018. *Ap. J. Lett.* 861(2):L17
- Lotz JM, Koekemoer A, Coe D, et al. 2017. *Ap. J.* 837:97
- Lovell CC, Vijayan AP, Thomas PA, et al. 2021. *MNRAS* 500(2):2127–45
- Ma X, Hopkins PF, Kasen D, et al. 2016. *MNRAS* 459(4):3614–19
- Ma X, Quataert E, Wetzel A, et al. 2020. *MNRAS* 498(2):2001–17
- Madau P. 1995. *Ap. J.* 441:18
- Madau P. 2017. *Ap. J.* 851:50
- Madau P, Dickinson M. 2014. *Annu. Rev. Astron. Astrophys.* 52:415–86
- Madau P, Haardt F. 2015. *Ap. J. Lett.* 813:L8
- Madau P, Haardt F, Rees MJ. 1999. *Ap. J.* 514(2):648–49
- Mainali R, Kollmeier JA, Stark DP, et al. 2017. *Ap. J. Lett.* 836:L14
- Mainali R, Zitrin A, Stark DP, et al. 2018. *MNRAS* 479:1180–93
- Maiolino R, Carniani S, Fontana A, et al. 2015. *MNRAS* 452:54–68
- Malkan MA, Alavi A, Atek H, et al. 2021. *PASSAGE-Parallel Application of Slitless Spectroscopy to Analyze Galaxy Evolution*. JWST Proposal. Cycle 1
- Marchi F, Pentericci L, Guaita L, et al. 2017. *Astron. Astrophys.* 601:A73
- Marchi F, Pentericci L, Guaita L, et al. 2018. *Astron. Astrophys.* 614:A11
- Mashian N, Oesch PA, Loeb A. 2016. *MNRAS* 455(2):2101–9
- Mason CA, Naidu RP, Tacchella S, Leja J. 2019. *MNRAS* 489(2):2669–76
- Mason CA, Trenti M, Treu T. 2015. *Ap. J.* 813:21
- Mason CA, Treu T, Dijkstra M, et al. 2018. *Ap. J.* 856:2
- Matsuoka Y, Onoue M, Kashikawa N, et al. 2016. *Ap. J.* 828:26
- Matsuoka Y, Strauss MA, Kashikawa N, et al. 2018. *Ap. J.* 869(2):150
- Matthee J, Sobral D, Best P, et al. 2017. *MNRAS* 465(3):3637–55
- Mauerhofer V, Verhamme A, Blaizot J, et al. 2021. *Astron. Astrophys.* 646:A80
- McGreer ID, Mesinger A, D'Odorico V. 2015. *MNRAS* 447:499–505
- McLeod DJ, McLure RJ, Dunlop JS. 2016. *MNRAS* 459(4):3812–24
- McLeod DJ, McLure RJ, Dunlop JS, et al. 2015. *MNRAS* 450(3):3032–44
- McQuinn M. 2016. *Annu. Rev. Astron. Astrophys.* 54:313–62
- Meneghetti M, Natarajan P, Coe D, et al. 2017. *MNRAS* 472(3):3177–216
- Meštrić U, Ryan-Weber EV, Cooke J, et al. 2020. *MNRAS* 494(4):4986–5007
- Meyer RA, Kakiuchi K, Bosman SEI, et al. 2020. *MNRAS* 494(2):1560–78
- Meyer RA, Laporte N, Ellis RS, Verhamme A, Garel T. 2021. *MNRAS* 500:558–64
- Mitra S, Choudhury TR, Ferrara A. 2015. *MNRAS* 454:L76–80
- Mitra S, Choudhury TR, Ferrara A. 2018. *MNRAS* 473:1416–25
- Monsalve RA, Rogers AEE, Bowman JD, Mozdzen TJ. 2017. *Ap. J.* 847:64
- Morishita T. 2021. *Ap. J. Suppl. Ser.* 253:4
- Morishita T, Stiavelli M, Trenti M, et al. 2020. *Ap. J.* 904:50
- Morishita T, Trenti M, Stiavelli M, et al. 2018. *Ap. J.* 867(2):150
- Mortlock DJ, Warren SJ, Venemans BP, et al. 2011. *Nature* 474(7353):616–19
- Mostardi RE, Shapley AE, Steidel CC, et al. 2015. *Ap. J.* 810(2):107
- Naidu RP, Forrest B, Oesch PA, Tran KVH, Holden BP. 2018. *MNRAS* 478:791–99
- Naidu RP, Tacchella S, Mason CA, et al. 2020. *Ap. J.* 892(2):109



- Shapley AE, Steidel CC, Strom AL, et al. 2016. *Ap. J. Lett.* 826(2):L24
- Sharma M, Theuns T, Frenk C, et al. 2016. *MNRAS* 458:L94–98
- Shen X, Hopkins PF, Faucher-Giguère CA, et al. 2020. *MNRAS* 495(3):3252–75
- Shipley HV, Lange-Vagle D, Marchesini D, et al. 2018. *Ap. J. Suppl. Ser.* 235:14
- Shivaei I, Reddy NA, Siana B, et al. 2018. *Ap. J.* 855:42
- Shull JM, Harness A, Trenti M, Smith BD. 2012. *Ap. J.* 747(2):100
- Siana B, Shapley AE, Kulas KR, et al. 2015. *Ap. J.* 804:17
- Smit R, Bouwens RJ, Labbé I, et al. 2014. *Ap. J.* 784:58
- Smith BM, Windhorst RA, Cohen SH, et al. 2020. *Ap. J.* 897:41
- Sobacchi E, Mesinger A. 2015. *MNRAS* 453(2):1843–54
- Song M, Finkelstein SL, Ashby MLN, et al. 2016a. *Ap. J.* 825:5
- Song M, Finkelstein SL, Livermore RC, et al. 2016b. *Ap. J.* 826(2):113
- Stanway ER, Eldridge JJ. 2018. *MNRAS* 479:75–93
- Stanway ER, Eldridge JJ. 2019. *Astron. Astrophys.* 621:A105
- Stanway ER, Eldridge JJ, Becker GD. 2016. *MNRAS* 456:485–99
- Stark DP. 2016. *Annu. Rev. Astron. Astrophys.* 54:761–803
- Stark DP, Ellis RS, Charlot S, et al. 2017. *MNRAS* 464:469–79
- Stark DP, Richard J, Charlot S, et al. 2015a. *MNRAS* 450(2):1846–55
- Stark DP, Schenker MA, Ellis R, et al. 2013. *Ap. J.* 763(2):129
- Stark DP, Walth G, Charlot S, et al. 2015b. *MNRAS* 454(2):1393–403
- Stefanon M, Bouwens RJ, Labbé I, et al. 2017. *Ap. J.* 843:36
- Stefanon M, Bouwens RJ, Labbé I, et al. 2021. *Ap. J.* 922:29
- Stefanon M, Labbé I, Bouwens RJ, et al. 2019. *Ap. J.* 883:99
- Steidel CC, Bogosavljević M, Shapley AE, et al. 2018. *Ap. J.* 869(2):123
- Strait V, Bradač M, Coe D, et al. 2020. *Ap. J.* 888(2):124
- Strom AL, Rudie GC, Chen Y, et al. 2021. *CECILIA: A direct-method metallicity calibration for Cosmic Noon through the Epoch of Reionization.* JWST Proposal. Cycle 1
- Sun G, Furlanetto SR. 2016. *MNRAS* 460:417–33
- Tamura Y, Mawatari K, Hashimoto T, et al. 2019. *Ap. J.* 874:27
- Tang M, Stark D, Chevallard J, et al. 2021. *MNRAS* 503(3):4105–17
- Tanvir NR, Laskar T, Levan AJ, et al. 2018. *Ap. J.* 865(2):107
- The HERA Collab., Abdurashidova Z, Aguirre JE, et al. 2022a. *Ap. J.* 294:51
- The HERA Collab., Abdurashidova Z, Aguirre JE, et al. 2022b. *Ap. J.* 295:221
- Tilvi V, Malhotra S, Rhoads JE, et al. 2020. *Ap. J. Lett.* 891:L10
- Tilvi V, Pirzkal N, Malhotra S, et al. 2016. *Ap. J. Lett.* 827:L14
- Topping MW, Shapley AE, Stark DP, et al. 2021. *Ap. J. Lett.* 917(2):L36
- Trenti M, Bradley LD, Stiavelli M, et al. 2011. *Ap. J. Lett.* 727(2):L39
- Treu T, Schmidt KB, Brammer GB, et al. 2015. *Ap. J.* 812(2):114
- Treu TL, Abramson LE, Bradac M, et al. 2017. *Through the Looking GLASS: A JWST Exploration of Galaxy Formation and Evolution from Cosmic Dawn to Present Day.* JWST Proposal ID 1324. Cycle 0 Early Release Science
- Ucci G, Dayal P, Hutter A, et al. 2021. *MNRAS* 506:202–14
- Vanzella E, de Barros S, Vasei K, et al. 2016. *Ap. J.* 825:41
- Vanzella E, Nonino M, Cupani G, et al. 2018. *MNRAS* 476:L15–19
- Vasei K, Siana B, Shapley AE, et al. 2016. *Ap. J.* 831:38
- Vielfaure JB, Vergani SD, Japelj J, et al. 2020. *Astron. Astrophys.* 641:A30
- Vijayan AP, Lovell CC, Wilkins SM, et al. 2021. *MNRAS* 501(3):3289–308
- Villasenor B, Robertson B, Madau P, Schneider E. 2021. *Ap. J. Accepted.* arXiv:2111.00019
- Vogelsberger M, Nelson D, Pillepich A, et al. 2020. *MNRAS* 492(4):5167–201
- Walter F, Decarli R, Aravena M, et al. 2016. *Ap. J.* 833:67
- Wang F, Davies FB, Yang J, et al. 2020. *Ap. J.* 896:23
- Wang F, Yang J, Fan X, et al. 2019. *Ap. J.* 884:30

- Wang F, Yang J, Fan X, et al. 2021. *Ap. J. Lett.* 907:L1
- Watson D, Christensen L, Knudsen KK, et al. 2015. *Nature* 519(7543):327–30
- Wechsler RH, Tinker JL. 2018. *Annu. Rev. Astron. Astrophys.* 56:435–87
- Wells M, Pel JW, Glasse A, et al. 2015. *Publ. Astron. Soc. Pac.* 127(953):646–64
- Wilkins SM, Feng Y, Di Matteo T, et al. 2016. *MNRAS* 458:L6–9
- Wilkins SM, Feng Y, Di Matteo T, et al. 2017. *MNRAS* 469(3):2517–30
- Williams CC, Curtis-Lake E, Hainline KN, et al. 2018. *Ap. J. Suppl. Ser.* 236(2):33
- Williams CC, Maseda M, Tacchella S, et al. 2021a. *UDF medium band survey: Using H-alpha emission to reconstruct Ly-alpha escape during the Epoch of Reionization.* JWST Proposal. Cycle 1
- Williams CC, Oesch P, Barrufet L, et al. 2021b. *PANORAMIC - A Pure Parallel Wide Area Legacy Imaging Survey at 1–5 Micron.* JWST Proposal. Cycle 1
- Willmer CNA, Hainline KN, Curtis-Lake E, Team JADES. 2020. In *Uncovering Early Galaxy Evolution in the ALMA and JWST Era*, ed. E da Cunha, J Hodge, J Afonso, L Pentericci, D Sobral, *Proc. LAU Symp.* 352, ed. E da Cunha, J Hodge, J Afonso, L Pentericci, D Sobral, pp. 356–58. Cambridge, UK: Cambridge Univ. Press
- Willott CJ, Abraham RG, Albert L, et al. 2017a. *CANUCS: The CANadian NIRISS Unbiased Cluster Survey.* JWST Proposal. Cycle 1
- Willott CJ, Arribas S, Ferruit P, Jakobsen P, Maiolino R. 2017b. *Cosmic reionization, metal enrichment and host galaxies from quasar spectroscopy.* JWST Proposal. Cycle 1
- Windhorst RA, Alpaslan M, Ashcraft T, et al. 2017. *JWST Medium-Deep Fields - Windhorst IDS GTO Program.* JWST Proposal. Cycle 1
- Wright GS, Wright D, Goodson GB, et al. 2015. *Proc. Astron. Soc. Pac.* 127(953):595
- Xu H, Wise JH, Norman ML, Ahn K, O’Shea BW. 2016. *Ap. J.* 833:84
- Yan H, Yan L, Zamojski MA, et al. 2011. *Ap. J. Lett.* 728:L22
- Yang J, Wang F, Fan X, et al. 2019. *Astron. J.* 157(6):236
- Yang J, Wang F, Fan X, et al. 2020. *Ap. J. Lett.* 897:L14
- Yue B, Castellano M, Ferrara A, et al. 2018. *Ap. J.* 868(2):115
- Yue B, Ferrara A, Xu Y. 2016. *MNRAS* 463(2):1968–79
- Yung LYA, Somerville RS, Finkelstein SL, Popping G, Davé R. 2019a. *MNRAS* 483(3):2983–3006
- Yung LYA, Somerville RS, Finkelstein SL, et al. 2020a. *MNRAS* 496(4):4574–92
- Yung LYA, Somerville RS, Popping G, Finkelstein SL. 2020b. *MNRAS* 494:1002–17
- Yung LYA, Somerville RS, Popping G, Finkelstein SL, Ferguson HC, Davé R. 2019b. *MNRAS* 490(2):2855–79
- Zackrisson E, Binggeli C, Finlator K, et al. 2017. *Ap. J.* 836:78
- Zackrisson E, Inoue AK, Jensen H. 2013. *Ap. J.* 777:39
- Zackrisson E, Rydberg CE, Schaefer D, Östlin G, Tuli M. 2011. *Ap. J.* 740:13
- Zheng W, Postman M, Zitrin A, et al. 2012. *Nature* 489(7416):406–8
- Zheng W, Zitrin A, Infante L, et al. 2017. *Ap. J.* 836(2):210
- Zhu H, Avestruz C, Gnedin NY. 2019. *Ap. J.* 882(2):152
- Zitrin A, Labb   I, Belli S, et al. 2015. *Ap. J. Lett.* 810:L12



Annual Review of  
Astronomy and  
Astrophysics

Volume 60, 2022

## Contents

Cosmology and High-Energy Astrophysics: A 50-Year Perspective on Personalities, Progress, and Prospects <i>Martin J. Rees</i> .....	1
Asteroseismology Across the Hertzsprung–Russell Diagram <i>Donald W. Kurtz</i> .....	31
Spirals in Galaxies <i>J.A. Sellwood and Karen L. Masters</i> .....	73
Galaxy Formation and Reionization: Key Unknowns and Expected Breakthroughs by the <i>James Webb Space Telescope</i> <i>Brant E. Robertson</i> .....	121
Atmospheres of Rocky Exoplanets <i>Robin Wordsworth and Laura Kreidberg</i> .....	159
Theory and Diagnostics of Hot Star Mass Loss <i>Jorick S. Vink</i> .....	203
Photodissociation and X-Ray-Dominated Regions <i>Mark G. Wolfire, Livia Vallini, and Mélanie Chevance</i> .....	247
The Cold Interstellar Medium of Galaxies in the Local Universe <i>Amélie Saintonge and Barbara Catinella</i> .....	319
Photometric Redshifts for Next-Generation Surveys <i>Jeffrey A. Newman and Daniel Gruen</i> .....	363
Magnetic Field Diagnostics in the Solar Upper Atmosphere <i>J. Trujillo Bueno and T. del Pino Alemán</i> .....	415
New Insights into the Evolution of Massive Stars and Their Effects on Our Understanding of Early Galaxies <i>Jan J. Eldridge and Elizabeth R. Stanway</i> .....	455
Pulsar Magnetospheres and Their Radiation <i>A. Philippov and M. Kramer</i> .....	495